10-15-2018

Theoretical Studies of Ultrafast Electron Dynamics in Atoms and Molecules via High-Order Harmonic Generation

Paul Vincent Abanador
Louisiana State University and Agricultural and Mechanical College, pabana1@lsu.edu

THEORETICAL STUDIES OF ULTRAFAST ELECTRON DYNAMICS IN ATOMS AND MOLECULES VIA HIGH-ORDER HARMONIC GENERATION

A Dissertation

Submitted to the Graduate Faculty of the
Louisiana State University and
Agricultural and Mechanical College
in partial fulfillment of the
requirements for the degree of
Doctor of Philosophy

in

The Department of Physics and Astronomy

by
Paul Vincent Abanador
B.S., De La Salle University, 2012
December 2018

Preface

Understanding the ultrafast motion of electrons is central to the study of atomic and molecular processes under intense laser fields. The natural time scale for the dynamics of bound electrons is a few hundred attoseconds (1 as = 10^{-18} s). For instance, the time it takes for a classical electron to complete its orbit around the hydrogen Bohr atom is about 150 as. In contrast, the vibrational motion of nuclei in molecules has a characteristic time scale of tens to hundreds of femtoseconds (1 fs = 10^{-15} s). From a fundamental perspective, the measurement and the control of ultrafast electron dynamics can have important implications for the early stages of chemical processes which occur on much longer time scales, including charge transfer and bond formation and breaking.

The strong-field process of *high-order harmonic generation* (HHG) provides access to an extremely broad bandwidth, which can be harnessed to produce ultrashort extreme-ultraviolet (XUV) pulses with sub-femtosecond duration. With the current advancements in ultrafast laser technology, the generation of these very short light pulses allows for time-resolved measurements of the attosecond dynamics of electrons. For a pump-probe scheme, a first femtosecond infrared (IR) pulse is typically used to initiate some dynamics in the atom or molecule, which can be later probed by a second, delayed HHG pulse. Furthermore, the HHG process itself has a natural attosecond time scale and can therefore be used in a self-probing scheme. This idea relies on the physical mechanism behind HHG, which can be intuitively described in terms of a recollision-based picture. In the presence of a strong, oscillating IR field, part of the electron bound state is released into the continuum and can be later driven back to the ionic core within one laser cycle. Here the rescattering electron wave packet acts as a self-probe for the structure and the dynamics of the ionic core. By characterizing the spectral amplitudes and phases of the emitted harmonics, the community envisions to retrieve information about the ultrafast electron dynamics.

The work that I have carried out during my PhD is mainly motivated by a large, multi-university collaboration for studying *charge migration*, which is a particular form of ultrafast electron dynamics. This collaboration involves both experimental and theoretical efforts for developing coherent probes of charge migration in molecules using strong-field ionization as well as HHG. In this thesis, we will focus on theoretical studies of different types of electron dynamics in atoms and molecules driven by intense laser pulses, via the process of HHG. The structure of this thesis is as follows. First, an introduction to essential concepts and methods in HHG theory is provided in Chapter 1. For the remaining chapters, we discuss our theoretical and numerical investigations, which are organized based on the approach used for treating the laser-matter interactions. In Chapter 2, we present the classical trajectory Monte Carlo method, wherein an ensemble of independent electron trajectories is propagated in the presence of an atomic argon potential and a strong laser field with elliptical polarization. In Chapter 3, we examine possible dynamical multielectron effects in molecules, which lead to the enhancement of HHG emission, from the numerical solution of the time-dependent Schrödinger equation for two active electrons each restricted to one dimension. Finally, in Chapters 4 and 5, we further explore the HHG process in more realistic molecular systems with multiple active orbitals using the time-dependent density functional theory approach.

My PhD work, including the studies presented in this thesis, has led to the following publications:

- F. Mauger, **P.M. Abanador**, K. Lopata, K.J. Schafer and M.B. Gaarde, *Semiclassical-wave-function perspective on high-harmonic generation*, Phys. Rev. A **93**, 043815 (2016).

- A. Sissay, **P. Abanador**, F. Mauger, M.B. Gaarde, K.J. Schafer and K. Lopata, *Angle-dependent strong-field molecular ionization rates with tuned range-separated time-dependent density functional theory*, J. Chem. Phys. **145**, 094105 (2016).

- **P.M. Abanador**, F. Mauger, K. Lopata, M.B. Gaarde and K.J. Schafer, *Semiclassical modeling of high-order harmonic generation driven by an elliptically polarized laser field: the role of recolliding periodic orbits*, J. Phys. B **50**, 035601 (2017).

- A. Bruner, S. Hernandez, F. Mauger, **P.M. Abanador**, D.J. LaMaster, M.B. Gaarde, K.J. Schafer and K. Lopata, *Attosecond charge migration with TDDFT: Accurate dynamics from a well-defined initial state*, J. Phys. Chem. Lett. **8**, 3991 (2017).

- F. Mauger, **P.M. Abanador**, A. Bruner, A. Sissay, M.B. Gaarde, K. Lopata, and K.J. Schafer, *Signature of charge migration in modulations of double ionization*, Phys. Rev. A **97**, 043407 (2018).

- **P.M. Abanador**, F. Mauger, K. Lopata, M.B. Gaarde and K.J. Schafer, *Wavelength and intensity dependence of recollision-enhanced multielectron effects in high-order harmonic generation*, Phys. Rev. A **97**, 043414 (2018).

- P. Sándor, A. Sissay, F. Mauger, **P. M. Abanador**, T. T. Gorman, T. D. Scarborough, M. B. Gaarde, K. Lopata, K. J. Schafer, and R. R. Jones, *Angle dependence of strong-field single and double ionization of carbonyl sulfide*, Phys. Rev. A **98**, 043425 (2018).

Table of Contents

Abstract

The interaction of atoms and molecules with strong laser pulses is of fundamental interest in physics and chemistry. Notably, the process known as high-order harmonic generation (HHG) refers to the production of extreme-ultraviolet (XUV) light, which occurs when an ensemble of atoms or molecules is subjected to a strong infrared laser field. Characterized by an attosecond time scale (1 as = 10^{-18} s), the HHG process provides the capability for experimental measurements to capture the ultrafast motion of electrons in these target atoms and molecules. The underlying physical mechanism behind this process naturally leaves imprints in the properties of the emitted XUV light, for instance, in the spectral amplitudes and phases. Within the single-atom or molecule description of HHG, we present theoretical and numerical studies based on (semi)classical and quantum approaches for treating the interactions with the long-range Coulomb and laser fields simultaneously in the electron dynamics. Using the classical trajectory Monte Carlo method, we examine the role of the atomic Coulomb potential in the single active electron dynamics responsible for the HHG process driven by an elliptically polarized laser field. Next, we apply quantum mechanical approaches to account for dynamical multielectron effects in molecular HHG. In particular, we numerically solve the time-dependent Schrödinger equation for a molecular model with two active electrons, each restricted to one dimension. Furthermore, we employ the time-dependent density functional theory approach to model the strong field dynamics of multiple active orbitals in more realistic full-dimensional molecular systems.

Chapter 1
Introduction

Strong-field physics is generally understood as the regime of light-matter interactions in which the laser light has an electric field strength comparable to that of the Coulomb field in atoms and molecules. When noble gases are irradiated with intense laser pulses (10^{13}–10^{16} W/cm^2), the emitted light contains odd harmonics of the fundamental frequency, which can go on to very high orders. This is a process known as *high-order harmonic generation* (HHG), which leads to the conversion of laser light from the visible or infrared to the extreme-ultraviolet (XUV) regime. A typical high-harmonic spectrum is shown in Fig. 1.1. In the case of an atomic target, only the odd harmonics can be observed in the HHG spectrum because of the inversion symmetry of the atom. The intensity of the first few (low-order) harmonics decreases rapidly with the harmonic order as one would expect from a perturbative response. As a signature of the nonperturbative nature of the laser-atom

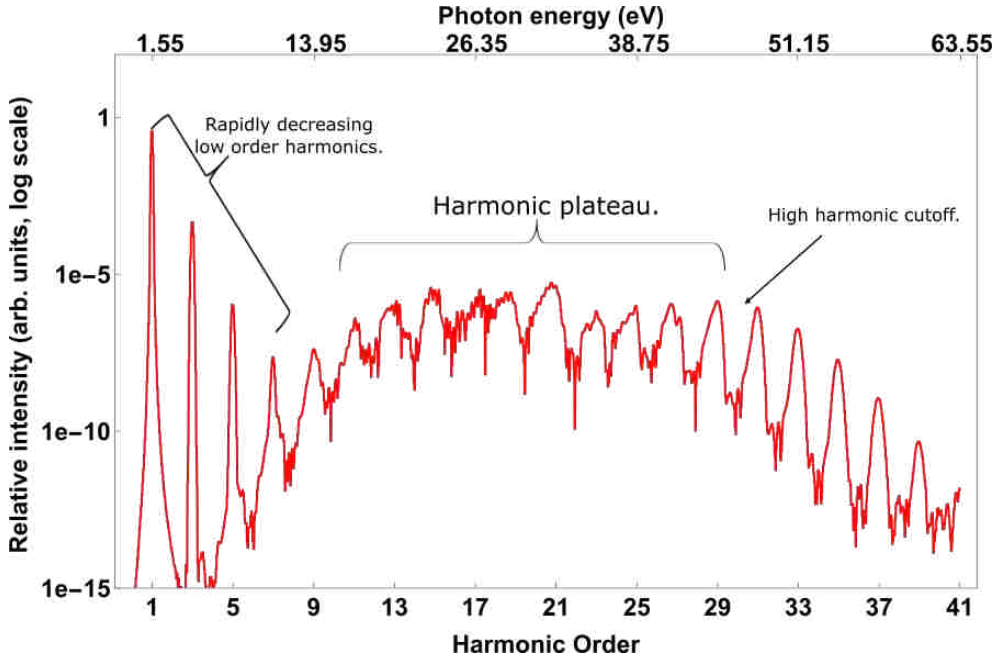

Figure 1.1: A typical high harmonic spectrum. This is obtained from a theoretical calculation for a single helium atom interacting with an 800-nm pulse (1.55 eV) with a peak intensity of 10^{14} W/cm^2.

interaction, the higher-order harmonics form a plateau wherein the harmonic intensity remains almost constant. This plateau extends up to a cutoff beyond which the harmonic intensity suddenly drops. The plateau in the HHG spectrum provides access to a large number of frequency components that roughly have the same intensity and that are mostly in phase. This is required for creating very short light pulses based on the inverse relation between the pulse length and bandwidth.

Since its discovery in the late 1980s [1, 2], HHG has become one of the most extensively studied phenomena in the strong-field regime because it is an important source of coherent XUV light [3, 4]. This technique has made possible the production of extremely short XUV pulses with duration less than a femtosecond (1 fs = 10^{-15} s) [5–8]. In addition, due to the short time scale involved in the HHG emission process, experimental measurements can now probe ultrafast electron dynamics on the natural time scale of attoseconds (1 as = 10^{-18} s) [9–11]. For instance, multielectron dynamics in atoms and molecules at the attosecond time scale have been characterized using high harmonic spectroscopy (HHS), which evaluates the information contained in the harmonic spectral amplitudes and phases [12–14]. Aside from probing the ultrafast electron dynamics itself, the motivation for studying the electronic motion within molecules is to provide insight towards the control of the subsequent nuclear motion which occurs on a longer time scale of tens to hundreds of femtoseconds [15]. In particular, the induced nuclear dynamics in molecules can lead to irreversible structural changes and ultimately chemical reactions [16]. Before delving into the numerical methods and the results of our study, we briefly discuss some fundamental concepts in current HHG theory.[1]

1.1 The Three-Step Model

The semiclassical (or recollision-based) model of HHG [17, 18] provides an intuitive picture of the process in terms of three steps in the interaction between an intense laser field

[1]Note that atomic units ($\hbar = m_e = e = a_0 = 1$) are used throughout this thesis unless otherwise stated.

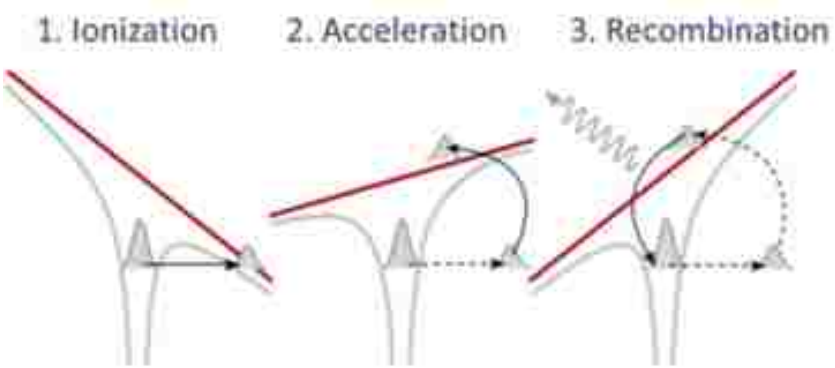

Figure 1.2: High-order harmonic generation (HHG) described in terms of three steps in the semiclassical model. The electron wave packet is shown in the combined potential due to the ionic core and the laser field at different stages in the HHG process. Reproduced from http://www.atomic.physics.lu.se.

and an electron bound in an atom or molecule, as illustrated in Fig. 1.2. This separation in the HHG process is reasonable because the three steps happen at very different time, energy and length scales. The electron tunnels through the barrier resulting from the combined laser and Coulomb fields (first step). The liberated electron then accelerates as it is driven mainly by the oscillating laser field (second step). Once the laser field reverses its direction, the electron may come back and recollide with the ionic core (third step). Since the electron "recombines" to its initial state, the third step leads to the emission of an HHG photon with energy $\Omega = I_p + E_r$. Here I_p is the ionization potential of the target atom or molecule and E_r is the return energy or the energy gained by the electron during its excursion from the moment of ionization to recombination.

Once the electron leaves the potential barrier, its dynamics becomes nearly classical because of the high density of states in the continuum and can therefore be described by electron trajectories usually called *quantum paths* or *orbits* [19]. The semiclassical model provides a map that links the emitted photon energies with particular electron trajectories, each characterized by its time of ionization (when it leaves the vicinity of the core) and its time of return to the core which determines its return energy. This model predicts that the generated harmonics will have energies between I_p and $I_p + 3.2U_p$, where $U_p = F_0^2/4\omega^2$ is the ponderomotive energy (the cycle-averaged quiver energy of an electron in an oscillating

field), and $3.2U_p$ is the maximum kinetic energy that the electron can gain during its motion in the laser field. Here F_0 and ω are the peak amplitude and frequency of the laser field, respectively. Thus, the ponderomotive energy U_p scales linearly with the laser intensity and quadratically with the wavelength. This corresponds to a semiclassical cutoff energy of $I_p + 3.2U_p$ in the HHG spectrum. To put this into perspective, a typical set of values for the laser intensity $I = 10^{14}$ W/cm^2 and wavelength $\lambda = 1$ μm corresponds to U_p of about 9 eV. Despite its simplicity, the semiclassical model predicts essential features of the HHG process such as the cutoff energy, which has been validated by more sophisticated calculations based on numerical and analytical solutions of the time-dependent Schrödinger equation (TDSE) for an atom interacting with a strong laser field [17, 20].

To further illustrate the semiclassical model, we consider a simple case where the driving laser field, given by $\mathbf{F}(t) = F_0 \cos(\omega t)\,\hat{\mathbf{x}}$, has linear polarization aligned along the x-axis. We apply the so-called *strong field approximation* (SFA) in which we assume that the electron dynamics in the continuum is influenced only by the laser field. Neglecting the effect of the Coulomb field after ionization, the classical equation of motion of the tunneled electron becomes

$$\ddot{x}(t) = -F_0 \cos(\omega t). \tag{1.1}$$

Here we assume that at some time t_i (ionization time), the electron is released into the continuum from the origin with an initial zero velocity. While the tunnel exit has a nonzero value, it can be taken to be zero in the first approximation. With strong driving fields, the electron excursion length is normally much larger than the size of the atomic ground state. This length scale for the electron motion is defined by the quiver amplitude $\alpha = F_0/\omega^2$, which increases with both the laser intensity and wavelength. For instance, the quiver amplitude is about 26 a.u. (14 Å) for the same laser parameters given before ($I = 10^{14}$ W/cm^2; $\lambda = 1$ μm).

Integrating Eq. (1.1) and applying the initial conditions $\dot{x}(t_i) = 0$ and $x(t_i) = 0$, we obtain

$$\dot{x}(t) = -\frac{F_0}{\omega}[\sin(\omega t) - \sin(\omega t_i)], \tag{1.2}$$

$$x(t) = \frac{F_0}{\omega^2}[\cos(\omega t) - \cos(\omega t_i)] + \frac{F_0}{\omega}\sin(\omega t_i)(t - t_i). \tag{1.3}$$

The first term in Eq. (1.3) corresponds to an oscillatory motion. Meanwhile, the second term corresponds to a linear motion with drift momentum that depends on t_i. This linear motion can dominate such that some electrons drift away from the parent ion without any recollision. Solving Eq. (1.3) numerically, we find some classical trajectories that travel in the laser field and that return to the origin at a later time t_r (recombination time) as shown in Fig. 1.3(a). Note that since we do not include the effect of the ionic potential as well as any initial momentum perpendicular to the laser polarization, the motion is one-dimensional. Electron trajectories with initial transverse momenta will most likely "miss" the atom and therefore will not contribute substantially to the HHG process. Satisfying the condition that trajectories do return to the ionic core, two classes of trajectories emerge from this recollision process: the so-called *short* and *long* trajectories. From the mapping of return energy versus recombination time in Fig. 1.3(b), we can clearly see the contributions

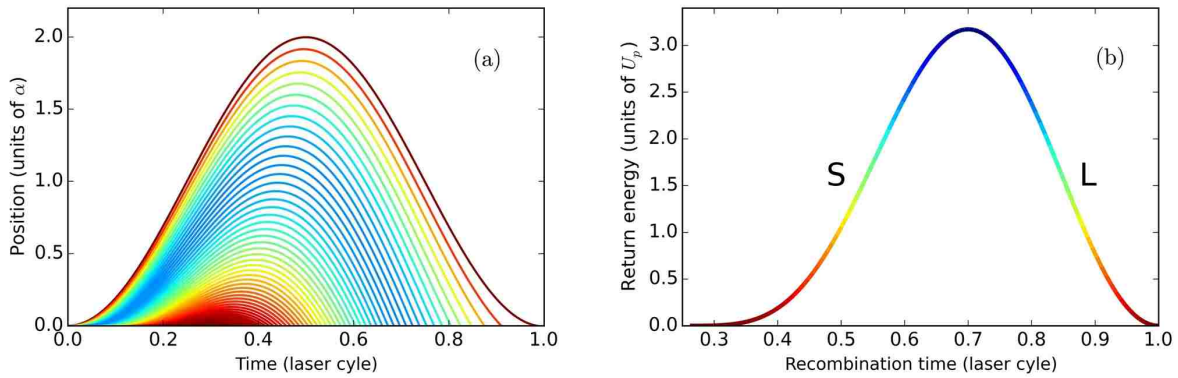

Figure 1.3: Semiclassical model of HHG. (a) Recolliding classical trajectories that are ionized at different times, from the peak of the field to 0.25 of the laser cycle. (b) Mapping of the return energy with respect to recombination time. The color of each trajectory in (a) corresponds to its return energy as indicated in (b), with two sets of returning trajectories labeled as short (S) and long (L) trajectories. The scales for the vertical axes in (a) and (b) are given in terms of the quiver amplitude α and the ponderomotive energy U_p, respectively.

from these sets of trajectories. Here we only consider the two shortest possible sets of trajectories, which are the short and long trajectories. They correspond to recolliding trajectories that return to the ionic core only once, within a laser cycle after ionization. For a given trajectory initialized at some time t_i, there may also be (subsequent) multiple returns, particularly when the excursion time considered is longer than one laser cycle.

In the strong field approximation the short and long trajectories arise from ionization at different times during the laser cycle, and they provide two possible pathways for the emission of an HHG photon with the same energy. The long trajectories, which are ionized near the peak of the field, travel in the continuum for a longer time than the short trajectories. Meanwhile, the short trajectories are ionized at 0.05–0.25 of the laser cycle after the peak of the field, and they return to the ionic core earlier than the long trajectories. The trajectory with travel time, $t_r - t_i$, of about 2/3 of the laser cycle corresponds to the maximal return energy of $3.2U_p$, which results in the well-known semiclassical cutoff energy of $I_p + 3.2U_p$.

So far we have examined the semiclassical picture, which is very simple and easy to implement. The next sections explore more formally the different aspects and implications of the three-step model as well as theoretical methods used for the microscopic (single-atom) description of the HHG process. In the last section we will also discuss macroscopic effects in order to provide some perspectives on how contributions due to different quantum paths in the single-atom emission of HHG can be separated in experiments.

1.2 Keldysh Theory and Tunnel Ionization

Historically, Keldysh (1964) [21] developed analytical methods for describing the interaction of atoms with intense fields in what would become one of the most influential papers in strong-field physics. The theoretical models for determining analytic solutions of atomic ionization rates developed by Perelomov, Popov, and Terentev (PPT) [22] and later extended by Ammosov, Delone, and Krainov (ADK) [23] are both based on the ground-

breaking work of Keldysh. Ionization by an intense laser field is the first step in the semiclassical model; therefore, the proper description of ionization within the laser cycle is imperative in the theoretical framework of HHG.

In his work [21], Keldysh introduced the dimensionless parameter $\gamma = \sqrt{I_p/2U_p}$ in order to characterize different mechanisms for ionization. The parameter γ is often interpreted as the ratio between the time it takes for the electron to cross the distance under the potential barrier, which is called the *Keldysh tunneling time*, and the time it takes for the laser field to lower this barrier. One approach for estimating the tunneling time is to consider a velocity $v = \sqrt{2I_p}$, which is associated with an electron that has binding energy $E = -I_p$. With this velocity, the electron has to travel across a barrier of length I_p/F_0 due to the laser field. In the adiabatic limit ($\gamma \ll 1$), ionization is described in terms of the *quasistatic tunneling* regime, where the electron travels through an essentially static potential barrier. This process gives an exponential dependence on the field amplitude for the ionization rate. On the other hand, the *multiphoton* regime takes place when $\gamma \gg 1$.

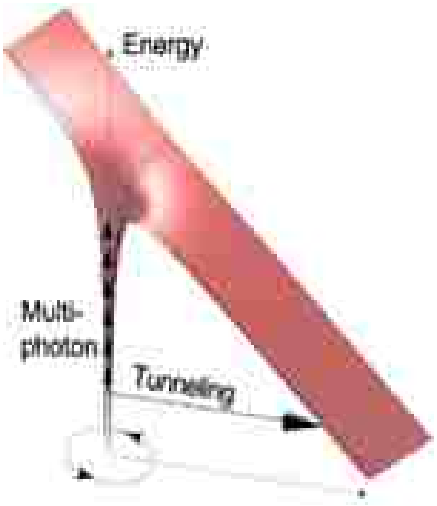

Figure 1.4: The potential due to the combined laser and Coulomb fields. The mechanisms for ionization in the Keldysh theory are typically interpreted as (1) multiphoton and (2) tunneling ionization as indicated by the "vertical" and "horizontal" channels, respectively. Adapted from [24] which is released under the Creative Commons Attribution 3.0 license.

Multiphoton ionization involves the absorption of several photons in order for the electron to escape from the atomic potential barrier. In this regime the barrier changes drastically during the tunneling process, leading to non-adiabatic effects that yield an I^n power law for the ionization rate with n the number of photons. These ionization mechanisms are depicted in Fig. 1.4.

Recently, new methods based on tunneling theory have been developed in order to predict strong-field ionization yields from molecules as a function of alignment angle between the molecular axis and the laser polarization. Analytical methods such as molecular ADK (MO-ADK) [25] and weak field asymptotic theory (WFAT) [26] both take into account the shape of molecular orbitals in the ionization process. An important feature that differentiates WFAT from MO-ADK is the inclusion of possible dipole effects, e.g., due to the permanent dipole moment of an unperturbed system, which is applicable to a polar molecule [26]. Advancements like these show the overall impact of the Keldysh theory in strong-field physics.

1.3 Strong Field Approximation

1.3.1 Formulation of the Lewenstein model

As an extension to the semiclassical model and tunneling theory, Lewenstein *et al.* [20] constructed a quantum-based approach for obtaining the HHG spectrum from a single atom, without solving the full quantum problem. The Lewenstein model, often interchangeably called the strong field approximation (SFA) model, provides an analytical solution of the TDSE under a set of assumptions that mimic the three-step model described earlier. For a single active electron (SAE) described by the wave function $\psi(\mathbf{r}, t)$, the TDSE in the length gauge reads

$$i\frac{\partial}{\partial t}\left|\psi(\mathbf{r},t)\right\rangle = \left[-\frac{1}{2}\nabla^2 + V(\mathbf{r}) + \mathbf{r}\cdot\mathbf{F}(t)\right]\left|\psi(\mathbf{r},t)\right\rangle, \tag{1.4}$$

where $V(\mathbf{r})$ is the atomic potential. The potential energy due to interaction with the driving laser field takes the form $\mathbf{r} \cdot \mathbf{F}(t)$ in the electric dipole approximation, where the size of the atom is assumed to be much smaller than the wavelength of the laser light.

The simplicity of the Lewenstein model is based on the following assumptions: (1) the contribution from only the ground state $|\psi_0\rangle$ is considered among all bound states, (2) the effect of the atomic potential is neglected in the continuum dynamics, and (3) the laser intensity is the below saturation level such that depletion of the ground state is ignored. In general, the assumption (2) is understood to be valid in the regime when the Keldysh parameter γ is small or in the tunneling regime. From these approximations the time-dependent wave function can be written as

$$|\psi(t)\rangle = e^{iI_p t}\left(\alpha(t)\,|\psi_0\rangle + \int d^3\mathbf{v}\beta(\mathbf{v},t)\,|\mathbf{v}\rangle\right), \tag{1.5}$$

where $\alpha(t)$ is the amplitude of the bound state, and $\beta(\mathbf{v},t)$ are the amplitudes of the continuum states $|\mathbf{v}\rangle$. In our discussion we set $\alpha(t) \cong 1$ although including effects due to the depletion of the ground state is straightforward (for example, see Ref. [27]). Each of the continuum states is labeled by its mechanical momentum $\mathbf{v}$, which is not a conserved quantity in the presence of an oscillating field. Here the ionized component of the wave function described by the continuum states can be represented by plane waves, consistent with ignoring the atomic potential after ionization. Again, let us consider the case where the linearly polarized laser field is along the x-axis (the same field in section 1.1). Since the mechanical momentum $\mathbf{v}$ varies in time, it is often convenient to define the canonical momentum $\mathbf{p} = \mathbf{v}(t) - \mathbf{A}(t)$ with the vector potential $\mathbf{A}(t)$. This canonical momentum is equal to the drift momentum, which is a conserved quantity in the free electron motion driven by the laser field.

The response of a single atom interacting with the driving laser field can be described by the time-dependent dipole moment $x(t) = \langle\psi(t)|\,x\,|\psi(t)\rangle$, which serves as the source term in the Maxwell wave equation (MWE) for calculating the generated electric field. By

taking the Fourier transform of $x(t)$, the radiation due to HHG that we are interested in can be found in the high frequency components of the induced dipole moment. Studying the properties of the time-dependent dipole moment therefore gives us insight into the emitted radiation (though this is not the whole story since there are macroscopic effects as well, see discussion in section 1.4). Inserting the expression of the wave function (1.5) into the TDSE (1.4), further analysis [20] yields

$$x(t) = -i \int_0^t dt' \int d^3\mathbf{p}\, F_0 \cos(t')\, d_x(\mathbf{p} + \mathbf{A}(t')) \exp[-iS(\mathbf{p}, t', t)]\, d_x^*(\mathbf{p} + \mathbf{A}(t)) \;+\; c.c., \quad (1.6)$$

where

$$S(\mathbf{p}, t', t) = \int_{t'}^t dt'' \left(\frac{1}{2}[\mathbf{p} + \mathbf{A}(t'')]^2 + I_p \right) \quad (1.7)$$

is the semiclassical action. The notation $\mathbf{d}(\mathbf{v}) = \langle \mathbf{v} | \, \hat{\mathbf{r}} \, | \psi_0 \rangle$ denotes the dipole matrix element for the bound-continuum transition while its component parallel to the polarization axis is denoted as $d_x(\mathbf{v})$. Since the integrand in the action (1.7) is the kinetic energy minus the potential energy, effects due to the atomic potential is included to some extent by the dependence on I_p. Note that each component in the integrand of Eq. (1.6) shows how the three-step model is recovered in the Lewenstein model. The factor $F_0 \cos(t')\, d_x(\mathbf{p} + \mathbf{A}(t'))$ is the probability amplitude associated with the part of the wave packet that is ionized at time t' with the canonical momentum $\mathbf{p}$. The ionized wave packet then acquires a phase $S(\mathbf{p}, t', t)$ as it travels in the continuum. Finally, the wave packet recombines to the ionic core at time t with the probability amplitude $d_x^*(\mathbf{p} + \mathbf{A}(t)) = \langle \psi_0 | \, \hat{\mathbf{x}} \, | \mathbf{p} + \mathbf{A}(t) \rangle$.

1.3.2 Saddle point analysis

The multidimensional integral in Eq. (1.6) can be very difficult to evaluate numerically over many quantum paths with various drift momenta, ionization times, and recombination times. In practice, its solution can be reduced to a set of quantum paths by applying the *stationary phase approximation* [28]. This approach relies on the destructive interference

of contributions from quantum paths with rapidly varying phases due to the semiclassical action (1.7). The HHG spectrum, which is proportional to the Fourier transform $\int x(t)e^{-i\Omega t}dt$, can therefore be derived approximately from quantum paths with phases

$$\tilde{S}(\Omega;\mathbf{p},t',t) = -\Omega t - \int_{t'}^{t} dt'' \left(\frac{1}{2}[\mathbf{p}+\mathbf{A}(t'')]^2 + I_p\right) \tag{1.8}$$

that are stationary with respect to the variables $(\mathbf{p},t',t)$.

The stationary solutions for $\mathbf{p}=\mathbf{p}_0$, $t'=t_i$, and $t=t_r$ are obtained from the saddle-point equations: $\nabla_{\mathbf{p}}\tilde{S}=0$, $\frac{\partial\tilde{S}}{\partial t'}=0$, and $\frac{\partial\tilde{S}}{\partial t}=0$. Thus,

$$\int_{t_i}^{t_r} dt''[\mathbf{p}_0+\mathbf{A}(t'')] = 0, \tag{1.9}$$

$$\frac{[\mathbf{p}_0+\mathbf{A}(t_i)]^2}{2} + I_p = 0, \tag{1.10}$$

$$\frac{[\mathbf{p}_0+\mathbf{A}(t_r)]^2}{2} + I_p = \Omega. \tag{1.11}$$

The integral in the left hand side of Eq. (1.9) corresponds to the electron displacement, and it is similar to setting $x(t_r)=0$ in Eq. (1.3) for a given trajectory initialized with drift momentum $\mathbf{p}_0$ at some time t_i. This means that the first equation (1.9) is equivalent to the condition for recollision imposed in the semiclassical model. The third equation (1.11) is simply a consequence of energy conservation for the emitted harmonic, whose energy is related to the kinetic energy of the returning wave packet. Note that, in the limit $\gamma=0$, the term I_p in Eq. (1.10) can be ignored since the energies of emitted electrons are much higher compared to I_p. In this limit the solutions for t_i and t_r become real-valued and the saddle-point equations simplify to the semiclassical model (see Fig. 1.3). Solving these equations for all possible sets of t_i and t_r and calculating the stationary phases of corresponding trajectories give the intensity and phase of the emitted radiation within the strong field approximation.

1.3.3 Factorization of the HHG spectrum

From the SFA formulation proposed by Lewenstein *et al.* [20], the single-atom HHG spectrum can be intuitively expressed as a product of the individual steps in the recollision model: the tunnel ionization probability, a phase function for the propagation, and the photorecombination cross section [12, 29, 30]. However, the approximate factorization of the harmonic yield within the SFA framework does not generally produce accurate results, e.g., when compared with the solution of the TSDE in the SAE approximation. Among the various factorization schemes that improve upon the SFA model, the *quantitative rescattering* (QRS) theory for HHG has been shown to be applicable for analyzing experimental measurements with molecular targets [31, 32]. In general, the validity of the QRS theory has been empirically demonstrated by the good agreement with results obtained from the SAE-TSDE approach for calculating HHG spectra [31, 33]. From the symmetry of simple linear molecules, the harmonic yield depends on the alignment angle θ, which is defined as the angle between the molecular axis and the laser polarization. In this case, the complex induced dipole $D(\Omega, \theta)$ from the QRS formulation is written as [34]

$$D(\Omega, \theta) = W(E_r, \theta) d(\Omega, \theta), \tag{1.12}$$

where $W(E_r, \theta)$ is the returning electron wave packet and $d(\Omega, \theta)$ is the transition dipole for the recombination back to the ground state. Based on the SFA model, the emitted harmonic energy Ω is related to the electron rescattering energy $\Omega = I_p + E_r$.

In the QRS framework [33], the harmonic yield is evaluated as $\mathcal{S}(\Omega) \sim |D(\Omega, \theta)|^2$, which gives a factorization in the energy domain. As a result, each step of the HHG process can be treated separately. The first component from the electron wave packet is the flux of returning electrons $|W(E_r, \theta)|^2$. The alignment-dependent ionization probability $N(\theta)$ can be introduced as an overall factor such that $|W(E_r, \theta)|^2 = N(\theta) |W'(E_r)|^2$, where $|W'(E_r)|^2$ is independent of the target system. The ionization probably $N(\theta)$ can be computed from various methods such as MO-ADK and WFAT. Furthermore, the returning wave packet

$W'(E_r)$ can be computed from the analytic SFA model or from the numerical solution of the SAE-TDSE for a reference atom with the same ionization potential [33]. This assumes the quantity $W'(E_r)$ is mainly determined by the laser parameters, that is, it does not change for targets with similar ionization potentials. The second component in the HHG yield is the photorecombination cross section $|d(\Omega, \theta)|^2$, which depends only on the target system. Within the SFA model, the transition dipole is given by $\mathbf{d}(\mathbf{k}) = \langle \mathbf{k} | \hat{\mathbf{r}} | \psi_0(\theta; \mathbf{r}) \rangle$ where the continuum state $\langle \mathbf{k}|$ is described by a plane wave with momentum k satisfying the relation $k^2/2 + I_p = \Omega$. The "ground state" $\psi_0(\theta; \mathbf{r})$ is typically chosen be to the highest occupied molecular orbital (HOMO), consistent with the SAE approximation. Alternatively, the transition dipole can also be computed from established quantum chemistry techniques for a more accurate description of the continuum states [35, 36]. Although these techniques are originally used for calculating photoionization cross sections in molecules, photorecombination can be simply viewed as the inverse process of photoionization.

1.4 Macroscopic Effects

The theoretical methods we have discussed so far rely on the single-atom description of the HHG process. In experiments, the high-harmonic field is generated from a macroscopic number of atoms (or molecules) interacting with a strong laser field. This production of XUV light via HHG is typically achieved by placing a gas jet of target atoms close to the focus of a laser beam, which allows for the intensities that are needed in HHG. Thus, the measured HHG radiation comes from the collective response of individual emitters located at different positions in the interaction region. Aside from the microscopic response via the TDSE, the theoretical description of the entire harmonic generation process also requires the solution of the MWE for propagating and *phase matching* the emitted radiation through the gas medium. Phase matching refers to the condition in which the XUV fields being generated from atoms at different points along the forward direction are mostly in phase so that they interfere constructively. The coupled solution of the TDSE and the MWE can be

computationally expensive, so simplifications for the calculation of the single-atom response is often implemented, e.g., using the SFA model [37]. Within this comprehensive framework, the microscopic and macroscopic effects in the HHG process can be disentangled.

For the microscopic (single-atom) description of HHG, the time-dependent dipole moment computed from the numerical solution of the SAE-TDSE is in general very complicated since it contains contribution from different pathways leading to the emission of the same photon energy [38]. In the macroscopic spectrum, the high-harmonic radiation due to the different quantum paths, e.g., the short and long trajectories, can be preferentially selected using phase matching or can be spatially separated in the far-field spectrum [37]. Based on the semiclassical description of the microscopic HHG process, the phase of the atomic dipole radiation has an intrinsic intensity dependence [28]. In the SFA model, this dipole phase is given by the semiclassical action in Eq. (1.7), which is interpreted as the phase acquired by the electron during its motion driven by the laser field. In the limit where the Keldysh parameter $\gamma = 0$, the dipole phase ϕ_{dip} only depends on the contribution from the kinetic energy which is scaled by the ponderomotive energy, $\phi_{\text{dip}} = \alpha_j U_p/\omega$. This corresponds to a linear dependence on the laser intensity with the phase coefficient α_j for a given trajectory j.

Because the long trajectory spends a longer time in the continuum, it generally has a much larger phase coefficient α_j than the short trajectory. This implies that the long trajectory has a contribution with dipole phase that varies rapidly with the laser intensity while the phase for the short trajectory contribution varies slowly with the intensity. The difference in the intensity-dependent phase behaviors of the short and long trajectory has important implications in the macroscopic level. Intuitively, the atoms "experience" different intensities across the spatial profile of the focused laser beam. The spatial intensity variation of the driving field gives a curvature to the phase fronts of the generated harmonic field, especially for large α_j [39]. For certain experimental conditions, the harmonic generation from both the short and long trajectories can be optimized, mainly by chang-

ing the position of the gas medium relative to the laser focus [39–41]. In this case, the long trajectory contribution is spatially separated from the short trajectory contribution in the far field. Such practice has been utilized in recent experiments in order to study the properties of these two sets of trajectories separately [42, 43].

Chapter 2
Classical Trajectory Monte Carlo

The classical trajectory Monte Carlo (CTMC) method was initially designed to address problems in atomic collisions [44]. As in HHG, the combination of bound and unbound motion of the electron makes fully quantum calculations difficult. In the CTMC framework the initial electronic state of a hydrogen atom, for instance, is classically described in terms of an ensemble of Kepler orbits. Properties of interest (such as the charge transfer and ionization cross sections due to collision with a proton) are calculated as the statistical average from an ensemble of electron trajectories with various initial conditions. In general, classical and semiclassical approaches such as the CTMC method allow for a more intuitive interpretation of the underlying physics behind different phenomena compared to purely quantum mechanical approaches. Another advantage of (semi)classical approaches is their easy generalizability to higher-dimensional and multielectron systems [45, 46]. Consequently, the CTMC method has been extended to numerous applications in the strong-field regime of laser-atom interactions (for examples, see [47, 48]).

In this chapter we examine the implementation of the CTMC framework for modeling HHG using an elliptically polarized laser field, which is largely based on our work presented in Ref. [49]. This theoretical study is inspired by recent experimental HHG measurements, where the ellipticity dependence have been resolved into contributions due to the short and long trajectories [43]. From a fundamental standpoint, the laser ellipticity serves as a parameter in the HHG process and thus provides a stringent test of the semiclassical model based on recolliding trajectories. Within the CTMC framework, we study the sub-cycle dynamics of these recolliding trajectories while treating the interactions with the laser and the atomic potential equally, beyond the commonly used strong field approximation (SFA). In addition to statistical analysis, we also employ nonlinear dynamical tools in order to elucidate the global organization of the recollision dynamics in this strongly driven system.

2.1 Classical Description of an Atom

Before the dynamical properties of a classical atomic system can be investigated, the initial distribution of electron trajectories must be chosen. Here we revisit the formulation of the CTMC method for a hydrogen-like atom. First proposed by Abrines and Percival (1966) [44], the classical atom is commonly described in terms of a microcanonical distribution. In this framework the initial distribution of the electronic state, which is defined by its binding energy $E = -I_p$, is given by

$$\rho(\mathbf{r}, \mathbf{p}) = \frac{1}{k}\,\delta\left(H(\mathbf{r}, \mathbf{p}) - E\right), \tag{2.1}$$

where $\mathbf{r}$ and $\mathbf{p}$ are the electronic coordinates in phase space, k is a normalization constant, and H is the atomic Hamiltonian. For the case of a hydrogen-like atom, the (field-free) Hamiltonian is

$$H(\mathbf{r}, \mathbf{p}) = \frac{p^2}{2} - \frac{Z}{r} \tag{2.2}$$

with Z the effective core charge. The radial, $\rho(r, E)$, and momentum, $\rho(p, E)$, distributions are acquired by integrating the initial phase-space distribution (2.1) over all possible momenta and positions, respectively:

$$\rho(r, E) = \frac{16r^2}{\pi R_0^3}\left(\frac{R_0}{r} - 1\right)^{1/2}, \tag{2.3}$$

$$\rho(p, E) = \frac{32p^2}{\pi P_0^3}\left(\frac{p^2}{P_0^2} + 1\right)^{-4}. \tag{2.4}$$

For normalization, the parameters $R_0 = Z/\left|E\right|$ and $P_0 = \sqrt{2\left|E\right|}$ are defined. Notice that the radial distribution (2.3) extends only up to the classical turning radius R_0.

In order to better represent the quantum initial distribution, Hardie and Olson [50] later introduced a scheme based on a discrete set of microcanonical distributions. For this model the radial distribution is written as

$$\rho(r) = \sum_{i=1} c_{E_i}\rho(r, E_i), \tag{2.5}$$

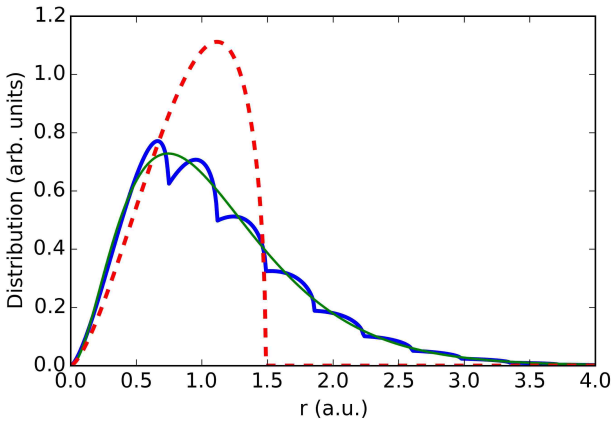

Figure 2.1: For a helium model atom ($Z = 1.345$), the radial distributions $\rho(r)$ obtained from a single microcanonical distribution (dashed curve) and from a linear combination of microcanonical distributions (thick solid curve) are shown. The quantum radial distribution is indicated by the thin solid curve.

where $\rho(r, E_i)$ is the radial distribution of the ith microstate. The coefficients c_{E_i} are obtained by fitting the radial distribution (2.5) to its corresponding quantum radial distribution, as illustrated in Fig. 2.1. For a hydrogen atom, the quantum radial distribution of the ground state is given by $r^2R(r)^2$, where $R(r)$ has an exponential dependence. Shown in Fig. 2.1, the quantum radial distribution for a helium model atom (thin solid curve) is determined from a scaled hydrogen-like atom with effective charge $Z = 1.345$. Since the expanded initial distribution (thick solid curve) mimics the associated quantum distribution, orbits that extend into the classically forbidden region are included. This in principle can improve the description of ionization due to strong fields. Indeed, compared to a single microcanonical distribution, the expanded description of the initial state has been demonstrated to ensure that classical and quantum ionization probabilities are in better agreement for a broad range of field intensities [51].

2.2 CTMC Framework: Elliptically Polarized Field

Utilizing the CTMC method, we explore the interplay between the laser and Coulomb fields in the HHG process for the case where the laser field has elliptical polarization. The

ellipticity of the driving laser field serves a "knob" that can be used in experiments in order to control the three-step recollision process. When driven by an elliptically polarized field, the initially ionized electron acquires a transverse displacement as it travels in the continuum and this suppresses the recollision process. Thus, the ellipticity dependence of harmonics generated from the short and long trajectory contributions naturally contain information about the continuum dynamics. As expected in the SFA model where the atomic potential is ignored, the accumulated transverse displacement due to the driving field can lead to a high sensitivity of the HHG process on laser ellipticity. Experimentally, it is well known that the harmonic yield is strongly suppressed when the ellipticity of the driving field is increased [52–55]. Although this dependence of the HHG yield on laser ellipticity has been extensively studied, the behavior of short and long trajectories in the presence of both the elliptically polarized laser and Coulomb fields remains an open question. By comparing our results from the CTMC approach with the SFA model, we are able to reveal the dynamics "beyond the standard model" of HHG.

Motivated by recent experimental measurements [43], we model HHG from an argon atom driven by an elliptically polarized field within the CTMC framework. For the propagation of classical trajectories, we use the Hamiltonian

$$\mathcal{H}(\mathbf{r},\mathbf{p},t) = H(\mathbf{r},\mathbf{p}) + \mathbf{r}\cdot\mathbf{F}(t) = \frac{p^2}{2} + V(r) + \mathbf{r}\cdot\mathbf{F}(t), \tag{2.6}$$

where $V(r)$ is the atomic potential, parameterized from the same calculation that yielded the quantum distribution for the initial state. The elliptically polarized driving field takes the form

$$\mathbf{F}(t) = \frac{F_0}{\sqrt{1+\varepsilon^2}}[\sin(\omega t)\hat{\mathbf{x}} + \varepsilon\cos(\omega t)\hat{\mathbf{y}}], \tag{2.7}$$

where F_0 and ε are the peak amplitude for linear polarization and the ellipticity of the laser field, respectively. Note that the cycle-averaged intensity in this form is independent of ε. From the Hamiltonian (2.6), we see that the CTMC method provides a description of

the electron dynamics where the atomic potential and the laser field interaction are treated on an equal footing, beyond the SFA model. The role of the atomic potential is generally expected to be significant in the intermediate regime between tunneling and multiphoton ionization, such that the Keldysh parameter $\gamma \approx 1$ [56]. For instance, the inclusion of the atomic potential has been found to have important implications for harmonics near the (ionization) threshold $\Omega = I_p$ [42, 57, 58].

Applying the three-step model, the HHG yield can be evaluated using the factorization $\mathcal{S}(\Omega) = W(\Omega)\sigma_{PR}(\Omega)$, where $W(\Omega)$ is the electron wave packet and $\sigma_{PR}(\Omega)$ is the photorecombination cross section (see discussion in section 1.3.3). The returning wave packet $W(\Omega)$, which accounts for both the ionization and propagation steps, is calculated from the flux of electrons that recollide with the ionic core in the CTMC framework [59]. When combined with a quantum mechanical representation for the recombination step, the CTMC method has been shown to (semi)quantitatively predict experimental measurements of the HHG spectra in Ar and Kr [59, 60]. Overall, the CTMC approach is summarized in terms of the following steps: (1) preparing the initial probability distribution of the system, (2) propagating the ensemble of classical trajectories, and (3) gathering the statistics of returning trajectories.

2.2.1 Initial state preparation

We implement the CTMC approach using the initial phase-space distribution discussed in section 2.1. Here the electronic state is represented in terms of a discrete phase-space distribution

$$\rho(\mathbf{r}, \mathbf{p}, t) = \frac{1}{\mathcal{N}} \sum_{j=1}^{\mathcal{N}} \delta(\mathbf{r} - \mathbf{r}_j(t))\delta(\mathbf{p} - \mathbf{p}_j(t)), \tag{2.8}$$

where $\mathcal{N}$ is the number of electron trajectories considered. For an initial radial distribution described in terms of m microcanonical distributions, we rewrite the expression (2.5) as

$$\rho(\mathbf{r}, t = 0) = \sum_{i=1}^{m} c_{E_i} \rho_M(E_i; \mathbf{r}, t = 0), \tag{2.9}$$

where each microcanonical radial distribution $\rho_M(E_i; \mathbf{r}, t = 0)$ takes the generalized form $C_i r^2 \sqrt{2[E_i - V(r)]}$ with C_i the corresponding normalization constants.

Preparing the initial phase-space distribution requires the proper application of the quantum-classical correspondence in the selection of both the range of initial energies and the angular momenta, as proposed in Ref. [61]. For the Ar $(3p)$ state, the microstate energies we use range from -1.885 to -0.150 a.u., and the classical angular momenta $|\mathbf{L}| = |\mathbf{r} \times \mathbf{p}|$ are restricted to lie between 1 and 2 in units of $\hbar$. The coefficients c_{E_i} are determined by fitting the radial distribution from the linear combination of 14 single microcanonical distributions to the quantum radial distribution from the solution of the Schrödinger equation using the Numerov algorithm [62]. To be precise, the radial part of Ar $(3p)$ state has a node near the origin. But since we are interested in classical trajectories that can be favorably ionized, the initial radial distribution is fitted such that it matches the quantum radial distribution only in the outer region. When determining the coefficients c_{E_i}, an additional constraint must be satisfied such that the ensemble average energy $\langle E \rangle_\rho = -I_p = -0.58$ a.u. for Ar $(3p)$.

2.2.2 Propagation of trajectories

Once an initial condition is chosen, each independent classical trajectory is propagated using Hamilton's equations:

$$\dot{\mathbf{r}}_j(t) \;=\; \mathbf{p}_j(t) \quad \text{and} \quad \dot{\mathbf{p}}_j(t) \;=\; -\nabla_{\mathbf{r}} V(r)|_{\mathbf{r}_j(t)} - \mathbf{F}(t) \tag{2.10}$$

from the Hamiltonian (2.6). Collectively, this corresponds to solving the temporal evolution of this dynamical system as dictated by the Liouville equation, which is the classical equivalent of the TDSE. For our calculations we perform the integration of trajectories in two spatial dimensions, corresponding to motion on a plane. The trajectories are allowed to propagate for the time interval $t \in [0, 3.25T_L]$, which accounts for returning trajectories that are ionized after the first laser half-cycle.

In the single-active-electron (SAE) approximation, the electron dynamics is limited to a single valence electron that experiences an effective atomic potential due to the nucleus

and other electrons. The model potential for Ar that we use was developed by Muller [63]:

$$V(r) = -\frac{1}{r} - \frac{Ae^{-Br} + (Z-1-A)e^{-Cr}}{r} \tag{2.11}$$

with optimized parameters $A = 5.4$, $B = 1$, $Z = 18$, and $C = 3.682$. This potential possesses a Coulomb tail $(-1/r)$ at the asymptotic region and the appropriate behavior $(-18/r)$ near the core. However, in practice, a small softening in the potential is introduced in order to remove the singularity at the origin.[1] This prevents spurious effects in the integration of trajectories.

2.2.3 Statistical analysis of returns

As proposed in the semiclassical model, the HHG process is attributed to electron trajectories that are ionized and later driven back to the ionic core. The rescattering wave packet $W(\Omega)$ is therefore described by the flux of returning electron trajectories. Here we identify returning trajectories as those that satisfy the condition: once it is ionized, the electron must enter a recombination sphere, which is centered on the target atom and has a radius R_{rec}. For example, Fig. 2.2(a) shows a typical returning trajectory that contributes to the total HHG yield. Note that the ionization time t_i and recombination time t_r are recorded at the instants when the electron leaves and enters the recombination sphere. For each returning trajectory, the total energy $E_r = p(t_r)^2/2 + V(R_{\text{rec}})$ and the angle θ_r, such that $\tan(\theta_r) = p_y(t_r)/p_x(t_r)$, are also computed. With access to individual trajectories, the short and long trajectories can be easily and clearly separated using the E_r versus t_r mapping as illustrated in Fig. 2.2(b).

Various properties of the dynamical system can be evaluated using the statistical distributions from an ensemble of classical trajectories. In this study we focus on the ellipticity dependence of the HHG process for short and long trajectories. For simplicity, in our analysis, we assume that the change in HHG yield due to the increase in ellipticity is pre-

[1] We substitute r with $\sqrt{r^2+\alpha^2}$ in the model potential (2.11) with $\alpha^2 = 5 \times 10^{-4}$ for the long-range Coulomb portion (first term) and $\alpha^2 = 10^{-3}$ for the short-range portion (second term).

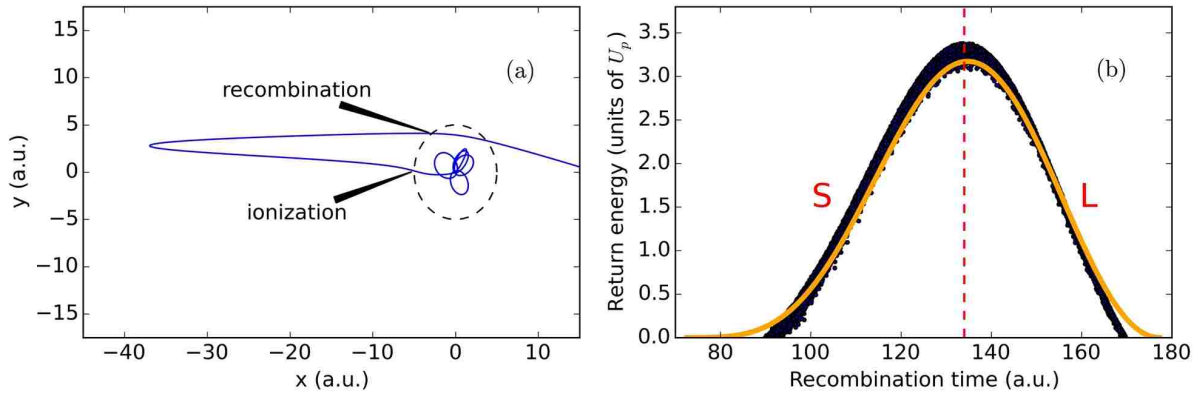

Figure 2.2: (a) Sample returning trajectory with return energy near the maximal value. The recombination criterion is satisfied when the electron comes back inside the recombination circle (dashed black curve) with radius of 5 a.u. (b) Statistical mapping of return energies E_r with respect to recombination times t_r for returning trajectories that are ionized in the first laser half-cycle of a linearly polarized laser field. The solid orange curve presents the corresponding prediction from the SFA model [similar to Fig. 1.3(b)]. The separation between short and long trajectories (vertical dashed line) is determined by the recombination time at which the return energy is maximal. Trajectories are calculated for laser intensity 8.5×10^{13} W/cm^2 and wavelength 1030 nm.

dominantly determined by the rescattering electron wave packet $W(\Omega)$. From a statistical standpoint, $W(\Omega)$ is acquired from the flux of returning trajectories

$$W(\Omega) = \frac{1}{\mathcal{N}} \sum_{j=1}^{\mathcal{N}_{\text{ret}}} f(E_{r,j}, \Delta E), \tag{2.12}$$

where $f(E_{r,j}, \Delta E)$ is a binning function such that

$$f(E_{r,j}, \Delta E) = \begin{cases} 1, & \text{if } |\Omega - E_{r,j} - I_p| < \Delta E/2 \\ 0, & \text{otherwise.} \end{cases} \tag{2.13}$$

The bin size is taken to be $\Delta E = 2\omega$ since only odd harmonics of the fundamental frequency ω are present in the spectrum experimentally. For statistical convergence, the total number of calculated trajectories for each ellipticity considered has been set at 10^6.

2.3 Effect of the Atomic Potential

We now proceed to the discussion of our results from the statistical analysis of returning trajectories in the CTMC approach. Particularly, we consider HHG from an Ar atom using a laser field with intensity 8.5×10^{13} W/cm^2 and a wavelength of 1030 nm, for varying ellipticity. These parameters are chosen for comparison with a recent experiment [43], where the HHG signal has been resolved into contributions due to the short and long trajectories from the microscopic description of the HHG process. For this experiment the Keldysh parameter is $\gamma = 0.97$, which is within the intermediate regime between tunneling and multiphoton ionization. Here we provide a discussion for the following cases: (1) linear and (2) elliptical polarization.

2.3.1 Linear polarization case

Already in the limiting case of linearly polarized driving laser field, we find nontrivial effects due to the inclusion of the atomic potential in our model. We compare our CTMC results with the SFA model (discussed in section 1.1), where the atomic potential is ignored after ionization. As shown in Fig. 2.2(b), the results from the SFA model and the CTMC method are in very good agreement in terms of E_r vs. t_r mapping. However, the underlying ionization mechanisms are not obviously seen from this E_r vs. t_r mapping. To identify these ionization mechanisms, we present the statistical mappings of recombination times and return energies versus ionization times, t_r vs. t_i and E_r vs. t_i in Figs. 2.3(a) and (b), respectively. A clear deviation from the standard SFA model is observed in the distribution of returning CTMC trajectories, where two prominent "branches" are found. These mappings suggest that the *late* trajectories, which correspond to the right branch in Fig. 2.3(a), have behavior or motion quite similar to SFA trajectories. By inspecting the dynamics of individual trajectories, we find that the late trajectories are nearly confined along the axis of the laser polarization, which we attribute to being ionized with small transverse momenta. Even though ionization in the CTMC framework is via a classical over-the-barrier

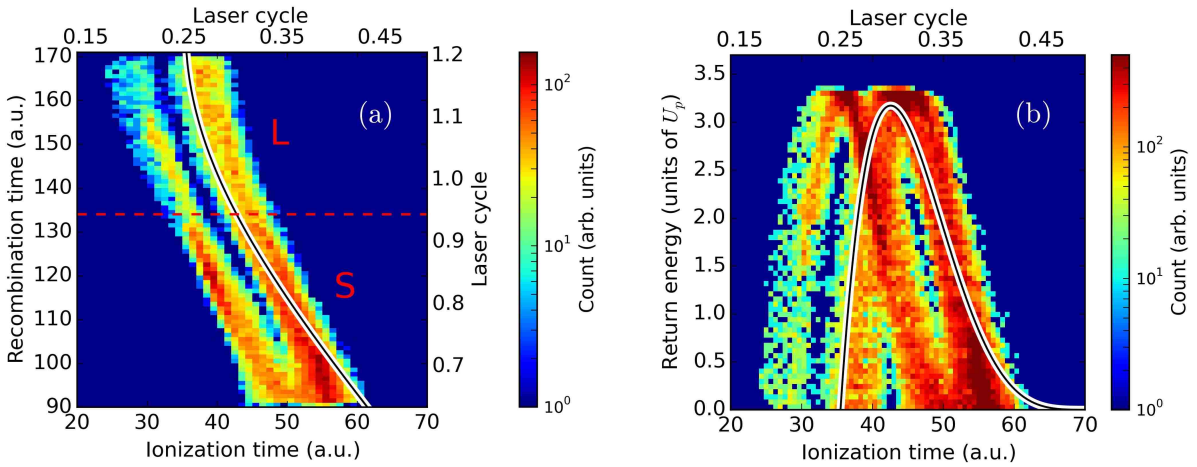

Figure 2.3: Distributions of ionization times t_i with respect to (a) recombination times t_r and (b) return energies E_r for the case of a linearly polarized laser field. The white-and-black curves indicate the mappings as predicted by the SFA model. For comparison, a scale in terms of the period of the laser field, which peaks at about 35 a.u. (or 0.25 laser cycle), is included. In both panels, only trajectories that return within a distance of 0.5 a.u. from the core are depicted in order to highlight the two branches, which are associated with two ionization channels (see text). Reprinted with permission from [49].

mechanism rather than quantum tunneling, the late trajectories mimic what we expect from the SFA trajectories after the electron leaves the core. This means that the exact ionization mechanism is not so important when analyzing the overall recollision dynamics.

From the left branch in Fig. 2.3(a), the returning trajectories can be seen to have ionization times that are about 10 a.u. (or 240 as) earlier than the SFA prediction. We refer to this set of returning trajectories as the *early* trajectories. The striking deviation from the SFA model emphasizes the role of the atomic potential for these returning trajectories. In contrast to the late trajectories, we find that the early trajectories are generally ionized with relatively large transverse momenta (perpendicular to the laser field) and are subsequently driven back to the ionic core with the aid of the Coulomb potential. Aside from inspecting individual trajectories, we also confirm the role of the atomic potential by turning it off in the propagation of trajectories once the electron leaves the recombination sphere. Indeed, we find that returns from the early trajectories are suppressed when the Coulomb potential is turned off (not shown).

2.3.2 Elliptical polarization case

Next we extend our analysis to the general case of an elliptically polarized laser field. Figure 2.4 presents the overall effect of ellipticity on the return angles of recolliding trajectories. Again, for comparison, we also display the return angles from the SFA model modified for the case with non-zero ellipticity. This is obtained by solving the equations of motion in two dimensions for the driving field given by Eq. (2.7). Starting from the origin with zero velocity, trajectories that do return to $x = 0$ never return to $y = 0$. Instead, the electron acquires a transverse displacement (along the minor polarization axis), which increases as it spends more time traveling in the laser field. In order for a given trajectory to come back to the origin, an initial transverse momentum must be chosen such that it compensates for the accumulated transverse displacement. Generally speaking, in our CTMC

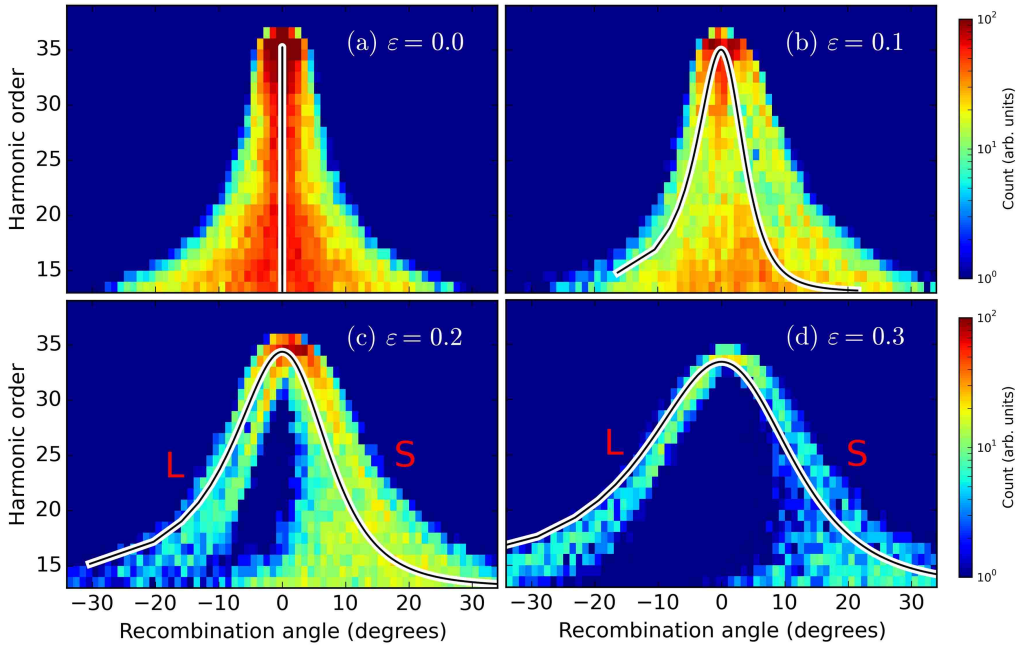

Figure 2.4: Distributions of return angles θ_r with respect to harmonic order of the photons emitted due to associated electron trajectories for ellipticity 0.0–0.3 (as labeled on each panel) using the similar selection of returning trajectories for Fig. 2.3. The white-and-black curves correspond to the mappings as predicted by the SFA model. The separation between the short (S) and long (L) trajectories is indicated in (c) and (d). Reprinted with permission from [49].

model there is no need to impose any initial condition for the ionization because effects due to both the laser and Coulomb fields are included in all steps of the HHG process.

The comparison between SFA and CTMC in Fig. 2.4 highlights the role played by the atomic potential in driving the recollision process. For linear polarization, the CTMC results show a much broader distribution of return angles compared with the SFA prediction especially in the region near the ionization threshold. As the ellipticity is increased, the contributions from short and long trajectories become separated, with return angles of opposite signs. For relatively high ellipticities (see the panels for $\varepsilon = 0.2$, 0.3 in Fig. 2.4), we see a broad agreement between the CTMC samples and the SFA model. However, Coulomb effects are revealed particularly for near-threshold long CTMC trajectories, whose distribution of return angles skews to lower values compared to those of SFA trajectories. This is in agreement with the Coulomb effects measured in experiments for HHG emission from the long trajectory [42]. Physically, the return angle of a trajectory is related to the polarization state (vector) of the emitted harmonic, which can be measured experimentally as an offset angle with respect to the main polarization axis of the driving field. Since the short and long trajectories recombine with the target system at different angles, the harmonic polarization angles are different (opposite signs) for these two sets of trajectories in the case of an elliptically polarized driving laser.

Furthermore, Coulomb effects can be seen to alter the recombination process for short trajectories, as evidenced by the broad distribution of return angles for ellipticities 0.2 and 0.3 in Fig. 2.4(c) and (d), respectively. The near-threshold short trajectories are associated with multiphoton processes as described in [58]. Since near-threshold short trajectories travel in a region near the core and they are ionized and driven back to the ionic core when the field is close to the zero of the field, the effect of the Coulomb potential is magnified. Altogether, these results so far indicate that additional pathways for returning trajectories arise from the inclusion of the Coulomb field.

2.4 Threshold Ellipticity

The sensitivity of the HHG yield with respect to the change in ellipticity of the driving field can provide insight into the sub-cycle dynamics of the ionized electron from the target atom. Experimentally, this dependence of the HHG process on the laser ellipticity is typically characterized using the threshold ellipticity, which is the ellipticity required for the harmonic intensity to be reduced to half of its value at linear polarization. Recently, experimental measurements of the threshold ellipticities for HHG in argon have been able to study the properties of the short and long trajectories separately [43]. As shown in Fig. 2.5, contributions from the short and long trajectory can be spatially separated at the "inner" and "outer" regions, respectively, of the HHG emission in the far field. The long trajectory contribution is more divergent compared to the short trajectory contribution since long trajectories have larger phase variations due to the intensity profile of the driving laser [39, 41, 64]. In their experiment [43], the phase matching conditions for harmonic generation from both the short and long trajectory are optimized mainly by adjusting the focusing geometry [40], i.e., placing the gas jet at the focus of the laser.

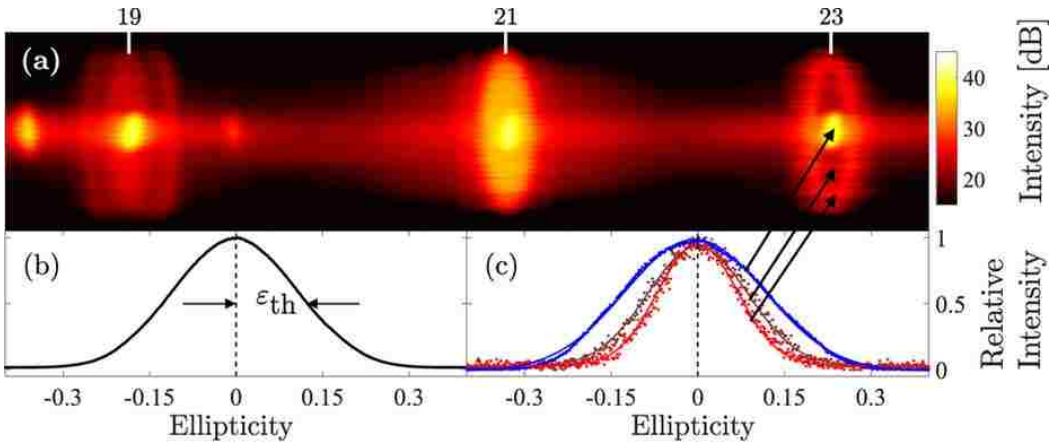

Figure 2.5: Harmonic spectrum under experimental conditions optimized to generate harmonics from both the short and long trajectories. (a) Spectral and spatial profile of HHG in the far field for linear polarization (harmonics 19–23 shown). (b) Ellipticity dependence of the spatially integrated signal of H23. (c) Extracted ellipticity dependence at three different regions in the spatial profile of H23. Adapted from [43] which is released under the Creative Commons CC BY license.

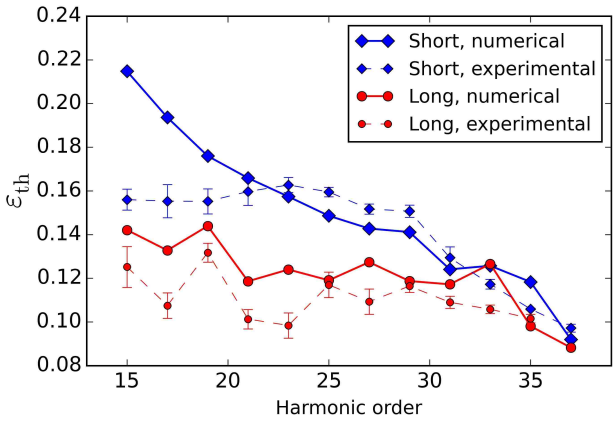

Figure 2.6: Comparison between numerically obtained results (solid lines) and measured data (dashed lines with smaller markers) for the threshold ellipticity $\varepsilon_{\mathrm{th}}$ as a function of harmonic order for the short (blue diamonds) and long (red circles) trajectories. The experimental results are taken from Ref. [43]. Reprinted with permission from [49].

In our CTMC calculations, the effect of the increase in laser field ellipticity is examined by calculating the HHG yield from the flux of returning trajectories, as indicated in Eq. (2.12). Here we consider electron trajectories that come back inside the recombination sphere of radius $R_{\mathrm{rec}} = 5.0$ a.u. From the obtained spectra at different ellipticities, the threshold ellipticity $\varepsilon_{\mathrm{th}}$ as a function of harmonic order is extracted for contributions from the short and long trajectories separately (see Fig. 2.6). For both the short and long trajectories, we find an overall trend where the threshold ellipticity $\varepsilon_{\mathrm{th}}$ decreases (or the HHG yield drops faster with increasing laser ellipticity) as the harmonic order increases. This means that trajectories that correspond to harmonics near the cutoff are more sensitive to the laser ellipticity than trajectories for low-order harmonics. The trends for both the short and long trajectories we find are in generally good agreement with the experimental results from Ref. [43], also plotted in Fig. 2.6. Noticeably, there is a difference between our CTMC results and the experimental results for the near-threshold short trajectories. This difference is probably to due effects not included in our model, for instance, macroscopic effects which go beyond the single-atom level.

Within the recollision scenario, we can interpret the observed trends in the threshold ellipticity. A lower (higher) threshold ellipticity means a higher (lower) sensitivity with

respect to increasing ellipticity, i.e., the HHG signal falls off more rapidly (slowly) as the ellipticity is increased. Thus, our results indicate that the near-threshold short trajectory harmonics are less sensitive to ellipticity than harmonics near the cutoff, which is consistent with previous studies [52, 54]. This behavior can be explained by noting that lower return energy for the short trajectory corresponds to spending less time in the continuum and therefore less spread in the wave packet along the transverse direction.

Looking at Fig. 2.6, we see that the same argument for the long trajectory does not necessarily hold. The near-threshold long trajectories, which travel in the continuum for a longer time than long trajectories with higher return energies, are expected to have more sensitivity (or lower ε_{th}). This counterintuitive sensitivity of the long trajectory has also been addressed and reproduced in Ref. [43] with ADK tunneling theory, which includes a field-dependent transverse momentum distribution for ionization. However, applying such tunneling conditions for the ionization step often becomes unreliable for the short trajectories possibly because they are ionized near the zero of the driving field. In our case we are able to reproduce decreasing trends from the experimental threshold ellipticities for both the short and long trajectories quite well. How can there be low-energy long trajectories with travel times close to a full cycle that are actually less sensitive to the ellipticity than long trajectories that have shorter travel times? In the following section we will show that the persistence of low-energy long trajectories can be understood in terms of so-called *recolliding periodic orbits* (RPOs), by applying techniques used in nonlinear dynamics. In particular, we will see that RPOs organize the recollision dynamics and that the low-energy long trajectories have very similar structures to weakly unstable RPOs, which are robust with respect to the increase in laser field ellipticity.

2.5 Recolliding Periodic Orbits

We go beyond the statistical analysis provided by the CTMC approach by shifting to an analysis based on nonlinear dynamical tools, specifically in terms of periodic orbits [65].

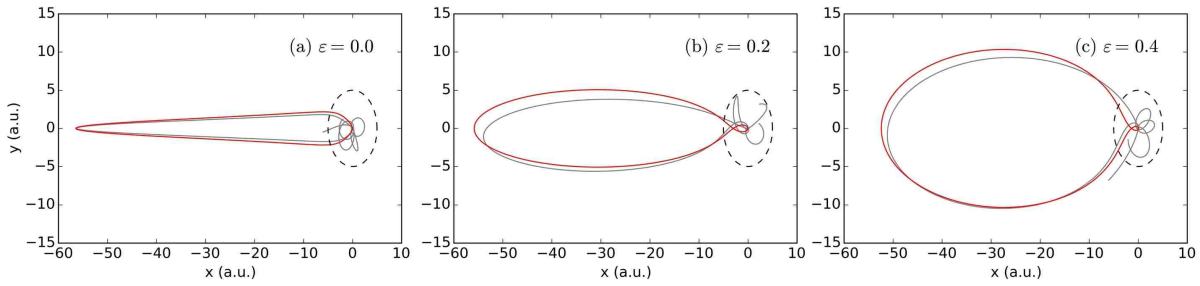

Figure 2.7: Recolliding periodic orbits (red curves) for ellipticities 0.0, 0.2, and 0.4 (as labeled on each panel). Each gray solid curve corresponds to a typical recolliding CTMC trajectory that mimics the shape of the RPO. The recombination sphere is represented with a dashed black curve in each panel. Reprinted with permission from [49].

Identifying pertinent periodic orbits has been demonstrated to provide a global picture for the dynamics in strongly driven systems [66, 67]. These periodic orbits are trajectories that repeat themselves in time, and they represent invariant structures for the dynamical system. In our study we are interested in recolliding periodic orbits (RPOs), which have been found to organize the way an electron can leave and find its way back to the ionic core [67]. Numerically, finding RPOs requires an iterative nonlinear solver for a trajectory such that it returns to its initial location in phase space after one laser cycle. The initial conditions for the nonlinear solver we use are actually from the positions and momenta of returning CTMC trajectories, providing an efficient way for the determination of relevant periodic orbits.

The best candidates for organizing the dynamics are the RPOs that have the same period as the laser field and that are weakly unstable [67]. In general, periodic orbits and their stability properties are robust with respect to small changes in the parameters of the dynamical system [68]. In this study we follow a set of RPOs as the ellipticity is increased, starting from the limiting case $\varepsilon = 0$. When the driving field is linearly polarized, Fig. 2.7(a) shows that the simplest RPO (red curve) corresponds to a single loop with large excursion away from the ionic core. The shape of this RPO changes as the ellipticity is increased as shown in panels (b) and (c). For different ellipticities, we find that low-energy long trajectories calculated from the CTMC method (gray curves) have striking resemblance

with the corresponding RPOs. We take this as strong evidence for the role of the RPOs in the global organization of the recollision dynamics.

These results suggest that we can use a nonlinear dynamical approach to examine the underlying mechanism responsible for the behavior of the long trajectory harmonics. To our knowledge, this is the first demonstration of the role of RPOs in regulating the dynamics responsible for HHG using elliptically polarized fields. Even at ellipticity higher than 0.2, the RPOs provide a map for electron trajectories to be initially ionized and to be driven back to the core with the aid of the atomic potential. The persistence of returning trajectories for relatively high ellipticities follows from the global organization of the dynamics by the RPOs. In particular, the RPOs explain how the low-order harmonic yield for long trajectories survives at these ellipticities. Since the RPOs travel in the continuum for about one laser cycle, they are more closely linked with near-threshold long trajectories. The long trajectories with higher return energies have shorter travel times; hence, the role of the RPOs becomes less prominent in the recollision process. In these distant regions the effect of RPOs is felt through their stable and unstable manifolds [69], which correspond to the pathways that a trajectory can return to and move away from the periodic orbit, respectively [65]. The overall influence of the RPOs is therefore connected to the associated HHG yields and the threshold ellipticity trends that we find.

Chapter 3
Numerical Solution of the Time-Dependent Schrödinger Equation

The solution of the time-dependent Schrödinger equation (TDSE) provides a fully quantum nonperturbative approach for describing fundamental processes in strong field physics. Unfortunately, the numerical integration of the full-dimensional TDSE is currently limited to cases with at most two electrons. From a theoretical standpoint, the inclusion of pertinent multielectron effects beyond the single active electron (SAE) approximation remains to be difficult, even for approximate solutions of the TSDE. In this chapter, we are interested in signatures of two-electron effects that can be found in molecular HHG, i.e., in the emitted light coming from the interaction of a single molecule with an intense laser field. Using a one-dimensional (1D) molecular model with two active electrons, we numerically demonstrate the enhancement of HHG emission due to the rescattering of the first electron to be ionized. By solving the TDSE for this molecular system in reduced spatial dimensions, we are able to systematically investigate the wavelength and intensity dependence of this recollision-enhanced HHG process. The two-electron effects we find in the calculated HHG spectra are related to the strong-field process commonly known as *nonsequential double ionization*. The methods and results presented in this chapter are largely based on our work in Ref. [70].

3.1 Mechanisms of Nonsequential Double Ionization

The semiclassical model has been widely proven successful in the physical interpretation of fundamental processes that pertain to the interaction of atoms and molecules with intense laser fields. Not only is the rescattering picture applicable to HHG, but it also explains the underlying mechanism behind other strong field processes, such as nonsequential double ionization (NSDI) [71–74] and above threshold ionization (ATI) [75–77]. Briefly, the NSDI process involves *inelastic rescattering* of an initially ionized electron which leads to another

electron being ionized from the parent ion. On the other hand, the ATI process involves *elastic rescattering* which leads to the release of a high energy photoelectron. In the case of NSDI, the theoretical description of the process requires electron-electron correlation, which facilitates energy exchange between the rescattering electron and the electrons left in the cation. This nonsequential physical mechanism is associated with the enhancement of double ionization yields compared to the predictions based on sequential ionization. The experimental evidence for NSDI was initially observed in xenon during the 1980s [78] and later also found in helium during the 1990s [79, 80]. The enhancement of double ionization due to the nonsequential mechanism is generally indicated by a "knee" structure in the intensity dependence of the double ionization yield. In particular, the He^{2+} yield for intensities below the saturation of the He^{+} yield is observed to be several orders of magnitude higher than what is expected from a sequential double ionization mechanism. In this sequential ionization model, the ionization of individual electrons is treated within the SAE approximation, that is, the electrons are assumed to be ionized one by one without any interaction with each other.

As we have discussed, the NSDI process is generally attributed to the three-step or recollision-based physical mechanism. When the first ionized electron is driven back to the ionic core, it may impart some of its kinetic energy to another electron which is also released from the binding potential due to the recollision. Hence, the NSDI process is understood to be the consequence of inelastic rescattering. Due to historical reasons, the term *nonsequential* double ionization is mostly used in the literature. Note however that this term broadly implies a *correlated* mechanism for the double ionization and that the two ionization events can be well separated in time. Apart from the recollision mechanism, other physical mechanisms were initially suggested to be responsible for NSDI. For example, the NSDI process was proposed to be the result of a "shake-off" mechanism, wherein the abrupt removal of the first ionized electron leads to the rearrangement of electrons left in the ionic core and consequently the promotion of the second electron to an excited state, from which

it is ionized [79]. In addition, the occurrence of NSDI has been theoretically modeled using a "collective tunneling" mechanism, wherein the two electrons are simultaneously released into the continuum via tunneling [81].

Later experiments have provided substantial evidence that supports rescattering as the basic mechanism behind the NSDI process. Similar to HHG, the NSDI yield is found experimentally to be suppressed with increasing laser field ellipticity [53]. Within the recollision picture, the initially ionized electron misses the ionic core because it accumulates a transverse displacement during propagation in the elliptically polarized driving field. Both the shake-off and collective tunneling mechanisms cannot explain this sensitivity of NSDI to the driving ellipticity. Perhaps even more convincing evidence for a recollision-based mechanism comes from the measurements using the cold target recoil-ion momentum spectroscopy (COLTRIMS) technique [82], which provides kinematic information of the double ionization process beyond the total ion yield. The first COLTRIMS experiments indicated that the distribution of doubly charged ion momenta parallel to the laser polarization are peaked at non-vanishing values [83, 84]. This implies that both electrons are preferentially released when the field is close to zero. Note that, in a sequential (uncorrelated) mechanism, each electron most likely enters the continuum when the field is maximal, which corresponds to a peak at vanishing momentum in the ion yield distribution.

Depending on the target system and the driving laser parameters, there are various physical mechanisms that are responsible for the release of two electrons. These underlying mechanisms are summarized in Fig. 3.1. As observed in the ion momentum distribution from the COLTRIMS experiments [83, 84], the double-peak structure at non-vanishing values is interpreted in terms of a recollision-driven mechanism. With a sufficiently high rescattering energy (determined by the U_p scaling), the initially ionized electron can directly knock out the second electron from the binding potential of the ionic core. This simple rescattering mechanism is called *electron-impact ionization* (shown middle in Fig. 3.1). In this case, both electrons can leave simultaneously close to a zero crossing of the driving field,

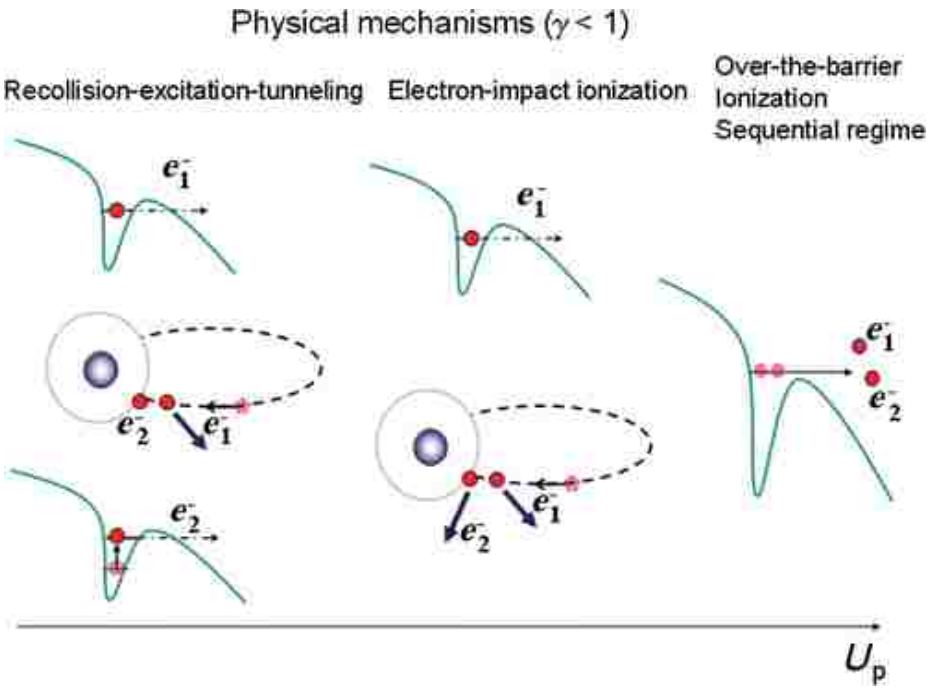

Figure 3.1: Dominant underlying mechanisms for double ionization due to strong fields. These mechanisms can be distinguished in terms of the energy scaling of the field-driven electron motion, which is determined by the ponderomotive energy U_p. Both the tunneling and over-the-barrier descriptions of ionization are assumed to be valid, particularly applicable to long driving wavelengths and high intensities (Keldysh parameter $\gamma \ll 1$). Reprinted with permission from [85].

which corresponds to "side-by-side" emission with non-vanishing drift momenta. From the correlated electron momentum distribution of NSDI, it is experimentally confirmed that the two electrons are emitted preferentially with the same parallel momenta [86]. Assuming zero initial electron momenta and ignoring the electron-electron Coulomb repulsion, the classical simpleman model predicts that both electron momenta distributions are peaked at values $\pm 2\sqrt{U_p}$.

Alternative routes towards recollision-driven double ionization have also been identified, notably the *recollision excitation with subsequent ionization* (RESI) [87, 88]. To illustrate the RESI mechanism (shown left in Fig. 3.1), the returning electron from the first ionization imparts some of its kinetic energy to its parent ion, which leads to the other electron being promoted to an excited state (recollision excitation). The second electron can later be released into the continuum, for instance, once the laser field is close to its maximum

(subsequent ionization). In contrast to direct impact ionization, there is an implied time delay between the recollision of the first electron and the ionization of the second electron. Thus, the RESI mechanism provides a pathway for "back-to-back" emission, which can describe the portions of the correlated momentum distribution in which the two electrons emerge with opposite parallel momenta. Specifically when the maximal rescattering energy does not exceed the second ionization potential of the target system, one can expect the RESI mechanism to be the dominant channel. Another possible scenario is when only one recollision is not enough to induce the second ionization event, that is, the first ionized electron is driven back to the ionic core multiple times. Such multiple-recollision mechanism has also been suggested to play an important role in the double ionization process [45, 89].

3.2 Numerical Details: Solving the TSDE

There is a variety of theoretical approaches that have been implemented in order to analyze atomic or molecular nonsequential double and multiple ionization. These approaches include the numerical solution of the TDSE, classical trajectory models, and extensions of the strong field approximation (for review papers, see [85, 90]). From the numerical solution of the TDSE for reduced-dimensional molecular models, two-electron dynamics reflected in HHG spectra have been investigated and analyzed for different internuclear distances [91]. We similarly employ a model molecular system with two active electrons, each restricted to one dimension ($1+1D$). Solving the TDSE in reduced spatial dimensions provides a practical approach for us to examine the wavelength dependence of HHG due to two-electron effects. For long driving wavelengths that we are interested in, the spatial grid typically needs to be adjusted (in each electronic coordinate) to account for the large electron excursion length, which scales as λ^2. Despite its simplicity, the $1+1D$ TDSE model has been widely used in theoretical investigations of various strong field phenomena. Most importantly, such reduced one-dimensional model has been instrumental in elucidating the recollision mechanism behind NSDI based on electron momentum distributions [92].

3.2.1 Molecular model in 1D

We consider a 1D molecular model (A_2) with two active electrons by solving the TDSE

$$i\frac{\partial}{\partial t}\Psi(x_1, x_2, t) = \hat{H}(x_1, x_2, t)\Psi(x_1, x_2, t). \tag{3.1}$$

Applying the length gauge and dipole approximation for the laser interaction, the Hamiltonian is given by

$$\hat{H} = \sum_{k=1}^{2}\left[-\frac{1}{2}\frac{\partial^2}{\partial x_k^2} + V_{\text{ne}}(x_k)\right] + V_{\text{ee}}(x_1, x_2) + (x_1 + x_2)F(t), \tag{3.2}$$

where V_{ne} is the electron-nucleus potential, V_{ee} is the electron-electron potential, and $F(t)$ is the driving laser field. To avoid the singularity, soft-Coulomb potentials [93] are introduced for the electron-nucleus and electron-electron interactions

$$V_{\text{ne}}(x) = -\frac{Z}{\sqrt{\left(x + \frac{R}{2}\right)^2 + a_{\text{ne}}^2}} - \frac{Z}{\sqrt{\left(x - \frac{R}{2}\right)^2 + a_{\text{ne}}^2}} \tag{3.3}$$

and

$$V_{\text{ee}}(x_1, x_2) = \frac{1}{\sqrt{(x_1 - x_2)^2 + a_{\text{ee}}^2}}, \tag{3.4}$$

where Z is the effective charge, R is the separation distance between the nuclei, and a_{ne} and a_{ee} are the softening parameters. In our study the positions of the nuclei are assumed to be fixed during the time propagation. The parameters for the 1D A_2 molecule are chosen to be $Z = 1$, $R = 1.9$ a.u., $a_{\text{ne}}^2 = 0.7$, and $a_{\text{ee}}^2 = 1$. This gives the following values of the ionization potentials, $I_p^{(1)} = 21.1$ eV for the A_2 molecule (first ionization) and $I_p^{(2)} = 38.9$ eV for its cation A_2^+ (second ionization). Note that, compared to the atomic case ($R = 0$), the difference between the first and second ionization potentials is smaller.

In our discussion we analyze and identify possible two-electron effects present in the HHG process by comparing the results from the A_2 TAE model to an effective SAE model. The temporal evolution of the molecular system, within the SAE approximation, is deter-

mined by a single-electron wave function $\psi(x,t)$ such that

$$\begin{aligned} i\frac{\partial}{\partial t}\psi(x,t) &= \hat{H}_{\rm eff}^{\rm SAE}(x,t)\psi(x,t) \\ &= \left[-\frac{1}{2}\frac{\partial^2}{\partial x^2} + V_{\rm eff}^{\rm SAE}(x) + xF(t)\right]\psi(x,t). \end{aligned} \tag{3.5}$$

Here the effective SAE potential $V_{\rm eff}^{\rm SAE}(x)$ is obtained using the same form as in Eq. (3.3). In particular, the parameters are adjusted ($Z = 0.5$ and $a_{\rm ne}^2 = 0.4235$) to match the first ionization potential of the two-electron A_2 molecular system. For both the TAE and SAE calculations, the solution of the TDSE is initialized from the ground state of the respective system. These calculations are implemented using the grid-based quantum code, OCTOPUS [94].[1] We ensure that our results are converged with respect to the numerical grid discretization, e.g., by applying sufficiently small grid spacing $\Delta x = 0.4$ a.u. (in each electron coordinate) and time step $\Delta t = 0.03$ a.u.

To examine the physics behind potential two-electron effects in the 1D molecular model used here, we calculate HHG spectra for a wide range of laser intensities and wavelengths. In our calculations we use a linearly polarized driving field, $F(t) = F_0\, f(t) \sin(\omega t)$, with an envelope

$$f(t) = \begin{cases} 0, & t < 0 \\ \sin^2(\pi t/2\tau), & 0 \le t \le \tau \\ 1, & t > \tau. \end{cases} \tag{3.6}$$

We use $\tau = 4\pi/\omega$ so that the envelope ramps up during the first two laser cycles and remains constant afterwards. This "flat-top" field envelope gives a well defined peak amplitude for the later cycles, which allows for a simple interpretation in terms of the maximal rescattering energy ($\approx 3.2U_p$). For HHG driven by long wavelengths, the associated returning trajectories classically extend at very large distances, i.e., up to about twice the quiver amplitude α [see Fig. 1.3(a)]. Thus, we use a spatial grid with an extent larger than

[1] In the next chapter, we provide a more detailed discussion of the Octopus code in the context of full-dimensional calculations. We also refer the reader to the online documentation for specific features.

the electron excursion length. In addition, to prevent effects due to unphysical reflections at the edges of the grid, absorbing boundaries are incorporated using a complex absorbing potential [95]. By sufficiently increasing the grid extent, we are able to significantly reduce the noise level due to reflections such that it is much lower compared to the signal from the two-electron effects we are interested in.

3.2.2 Calculation of HHG spectra

For the two-electron molecular system, the (total) time-dependent dipole moment and dipole acceleration are evaluated as

$$d(t) = \langle x_1 + x_2 \rangle = \langle \Psi(t) | \, x_1 + x_2 \, | \Psi(t) \rangle \tag{3.7}$$

and

$$a(t) = \frac{\mathrm{d}^2}{\mathrm{d}t^2} \langle x_1 + x_2 \rangle = \left\langle \Psi(t) \middle| -\frac{\partial V(x_1, x_2)}{\partial x_1} - \frac{\partial V(x_1, x_2)}{\partial x_2} \middle| \Psi(t) \right\rangle, \tag{3.8}$$

respectively. The expression of the dipole acceleration follows from the Ehrenfest's theorem for electrons experiencing the potential $V(x_1, x_2)$. The corresponding HHG spectrum is then computed from the Fourier transform of the dipole moment or dipole acceleration. Note that calculating the dipole moment gives more weight to the density at distances far away from the ionic core, whereas calculating the dipole acceleration gives more weight to the density near the ionic core. The agreement between these two ways for acquiring the HHG spectrum is usually checked to test the quality of the spatial grid used. In practice, it has been shown that using the dipole acceleration results in a more numerically exact computation of the harmonic spectrum [96]. We also apply a Hanning window function [97] to the time signal from our calculations over a duration of several laser cycles. Such window functions make the time signal go smoothly to zero at both ends and, in general, prevent spurious frequencies associated with a discrete Fourier transform used for analyzing the time signal. In addition to calculating HHG spectra, we employ a time-frequency analysis

of the dipole acceleration using the Gabor transform [98] defined as

$$a_G(\Omega, t) = \int dt' a(t') \frac{\exp\left[-(t'-t)^2/2\sigma^2\right]}{\sigma\sqrt{2\pi}} \exp\left(-i\Omega t'\right), \tag{3.9}$$

where the standard deviation for the Gaussian window function is set as $\sigma = 1/(4\omega)$ or about 4% of the laser cycle. Performing the Fourier transform over a small window provides a way to resolve the "emission time" for various harmonics throughout the spectrum.

3.3 Recollision-Enhanced HHG Process

Based on the numerical techniques presented in the previous section, we discuss the results from the 1D A_2 molecular model. From the solution of the TDSE for two active electrons, we explore the enhancement of the HHG yield due to rescattering of the first ionized electron. To demonstrate this effect, we first show the results for the case with laser wavelength equal to 1400 nm and peak intensity equal to 5×10^{13} W/cm^2 (see Fig. 3.2). Here the laser intensity is chosen such that it is well below the saturation intensity for the first ionization. From Fig. 3.2, we observe that there are two noticeable plateaus and cutoffs in the harmonic spectrum generated from the A_2 TAE model (solid red). Indicated by the vertical dashed lines, we see (1) a primary cutoff at about 55 eV and (2) a secondary cutoff at about 72 eV. The first plateau and cutoff from the A_2 TAE model is generally in good agreement with the spectrum generated from the A_2 SAE model (dashed blue). This indicates that the primary cutoff can be attributed to the dynamics of the first ionized electron. The position of the primary cutoff is rather consistent with the estimated cutoff energy from the semiclassical model, $I_p^{(1)} + 3.2U_p \approx 50$ eV. However, the returning electron can gain additional kinetic energy due to the potential of the ionic core [20], which explains the discrepancy between the actual and estimated cutoff energies.

Extending beyond the primary cutoff predicted by the A_2 SAE model, we additionally find a secondary cutoff in HHG spectrum from the A_2 TAE model shown in Fig. 3.2. Notice that the secondary cutoff matches the corresponding cutoff energy for HHG in the

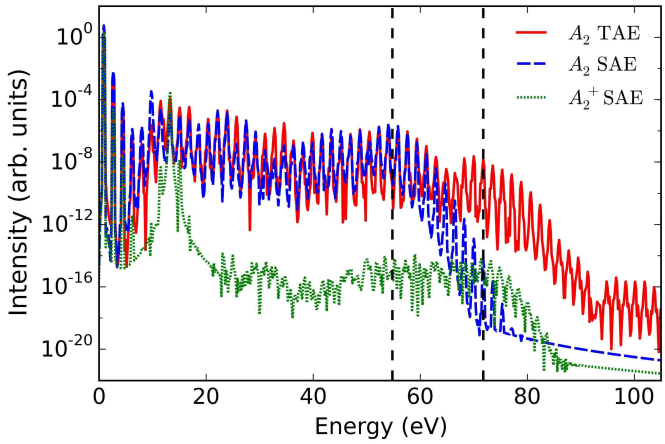

Figure 3.2: Harmonic spectra from the A_2 TAE (solid red) and SAE (dashed blue) molecule and from its corresponding cation A_2^+ (dotted green). These spectra are acquired from the time-dependent dipole acceleration over the duration of t = 3–8 laser cycles. For each system the simulation is initialized from its ground state. Here the driving laser field has a peak intensity of 5×10^{13} W/cm^2 and a wavelength of 1400 nm. The vertical dashed lines correspond to the first and second cutoffs. Reprinted with permission from [70].

A_2^+ cation, which is predicted to be $I_p^{(2)} + 3.2U_p \approx 68$ eV. From the dynamics of the two-electron wave function provided by the TDSE, contributions due to the singly ionized cation (A_2^+) are in principle also included [99]. To confirm the origin of the secondary cutoff, we also calculate the HHG spectrum initialized from the A_2^+ cation (dotted green). This involves solving the TDSE using the potential (3.3) for only one electron and thus we refer to it simply as the A_2^+ SAE model. Although the position of the secondary cutoff in the A_2^+ TAE molecule closely matches the result from the A_2^+ SAE cation, the observed HHG yields from the two models are very different. Surprisingly, there is an overall enhancement of several orders of magnitude in the HHG yield at the secondary plateau compared to the A_2^+ SAE model. These results suggest that two-electron effects included in the TSDE model lead to the large enhancement of HHG from the cation. In a sequential mechanism, one would expect that the HHG yield from the cation is predominately determined by the ionization probability from the ground state of the cation, which in turn give an HHG yield similar to the A_2^+ SAE model. Hence, we attribute the enhancement of HHG in the TAE neutral molecule to the correlation between the rescattering electron and the other electron

remaining in the cation. This mechanism for the enhancement of HHG due to rescattering has also been recently reported in a model atomic system [100].

The recollision-enhanced HHG process we find is similar to the well known enhancement of NSDI dominating over sequential double ionization. Using classical trajectory models, the underlying physical mechanisms related to double ionization have been investigated in great detail [101–105]. For instance, in Ref. [104], the optimal efficiency of NSDI has been interpreted in terms of the available energy provided by the rescattering electron. In the context of the RESI mechanism [105], the initially ionized electrons recollides with the cation and imparts some of its kinetic energy with the second electron left in the cation. Depending on the amount of energy exchanged between the two electrons, the cation may be left in an excited state. This mechanism enhances the second ionization probability and thus the respective HHG yield from the cation. We note that the available rescattering energies from the laser parameters considered in Fig. 3.2 are comparable to first excitation energy of the A_2^+ cation (13.3 eV), which is consistent with the RESI mechanism. In the following we will analyze the time-frequency profiles of the emission from the recollision-enhanced HHG process. Furthermore, we will provide insight into the wavelength and intensity dependence of the associated second-cutoff HHG yields.

3.3.1 Time-frequency analysis of the HHG emission

Using the Gabor analysis given by Eq. (3.9), we further substantiate the recollision mechanism behind the enhancement of HHG emmission in the secondary plateau and cutoff. We obtain the time-frequency profiles from the calculated HHG signals in order to visualize the emission times as well as the relative intensities of the first and second-cutoff harmonics. In Fig. 3.3, we compare the Gabor profiles of the harmonic emission from the (a) TAE and (b) SAE A_2 molecular models based on the results shown in the previous figure. Overall, we find that the position of the first cutoff is consistent for both models, as demonstrated in Fig. 3.2. Near the primary cutoff in both panels of Fig. 3.3, we can see distinct structures that are recurring every half-cycle after the field ramp-up at $t = 2$ laser cycles. This can

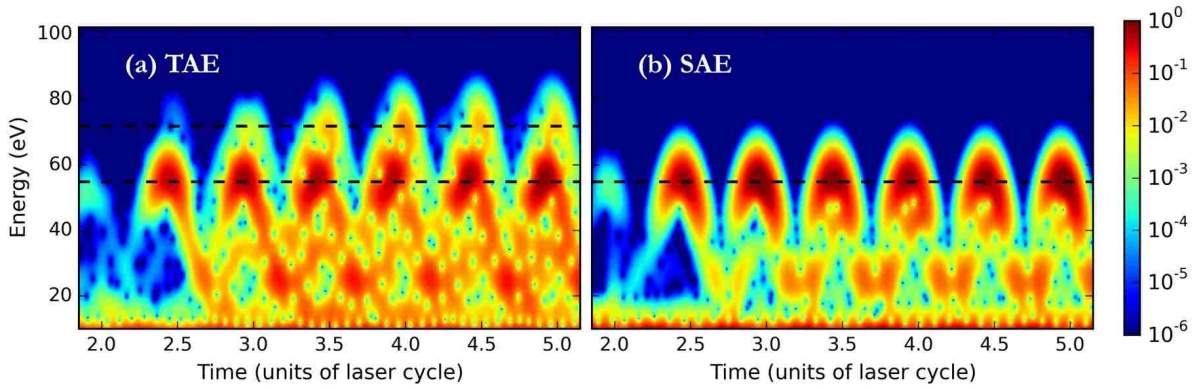

Figure 3.3: Gabor analysis of the HHG from A_2 molecule with the same laser parameters as in Fig. 3.2. The time-frequency profiles are obtained from (a) TAE and (b) SAE simulations. The horizontal dashed lines correspond to the first and second cutoffs (same as previous figure). Only the first cutoff is indicated in (b). Reprinted with permission from [70].

be understood in terms of the recollision mechanism which happens every half-cycle of the laser field. From the semiclassical model, the short and long trajectories are expected to merge in this cutoff region. Meanwhile, at lower energies in the primary plateau, there are overlapping structures that reflect contributions from different trajectories including multiple recollisions [106]. In our analysis, we therefore mainly focus on the harmonic emission close to the first and second cutoff energies.

From the A_2 TAE model in Fig. 3.3(a), we see that the harmonics in the primary cutoff are emitted with nearly constant yield starting from the first half-cycle after the field ramp-up. Beyond the first cutoff, we also observe the HHG emission in the secondary plateau, which is not visible in the SAE model as expected from the previous figure. Compared to the first-cutoff harmonics, the time it takes for the harmonic intensity near the secondary cutoff to reach a full value is delayed by several half-cycles. This delayed emission supports the recollision-enhanced mechanism for the HHG in the cation, in agreement with the time-frequency analysis from Ref. [100]. The secondary HHG process in the cation is triggered by the recollision of the first ionized electron, which is associated with the HHG emission in the neutral molecule. Therefore, the time delay between the first and second-cutoff emission is determined by the travel time of the second electron after being

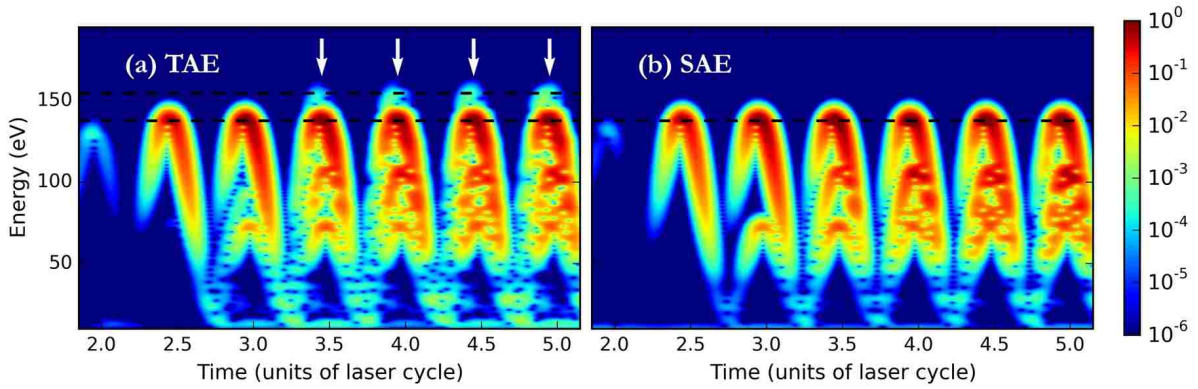

Figure 3.4: Gabor analysis of the HHG from A_2 molecule with the same laser peak intensity as in Fig. 3.3 but with a different wavelength, 2750 nm. The horizontal dashed lines for the first and second cutoffs are shown, similar to Fig. 3.3. The white arrows indicate emission at the second cutoff present in (a) TAE simulation but not in (b) SAE simulation. Reprinted with permission from [70].

ionized from the cation. For the harmonics generated in the secondary cutoff, the second electron has to travel in the continuum for about 2/3 of a laser cycle. This explains why the observed delay in the emission of the second-cutoff harmonics is more than half a laser cycle. Nevertheless, notice from Fig. 3.3(a) that there is already some weak emission in the second-cutoff harmonics starting at $t = 2.45$ laser cycles. In general, we attribute these residual second-cutoff yields to the recollisions of the first electron at earlier times during the ramp-up of the laser field.

Next, we examine how the recollision-enhanced HHG process is affected when the wavelength of the laser field is increased. In Fig. 3.4, we similarly display the time-frequency profiles of the harmonic generation from the (a) TAE and (b) SAE A_2 models, for a longer laser wavelength equal to 2750 nm. Here we fix the laser peak intensity at 5×10^{13} W/cm^2. This corresponds to about four times the ponderomotive energy U_p from the previous case shown in Fig. 3.3. For the longer wavelength case in Fig. 3.4(a), we also find emission of harmonics that are beyond the primary cutoff (see white arrows). Note that the position of the second cutoff relative to the first cutoff does not change with the driving wavelength. This is consistent with the recollision model of HHG, wherein the relative position of the second cutoff is determined only by the difference in the ionization potentials, $I_p^{(2)} - I_p^{(1)}$.

Comparing the results from Figs. 3.3(a) and 3.4(a), we observe that the secondary plateau has a much weaker relative yield in the case with longer wavelength. In Fig. 3.4(a), there is almost no second-cutoff HHG yield that is present during the first cycle after the field ramp-up. In contrast to the shorter wavelength case, we can clearly see that the emission of the second-cutoff harmonics is delayed by a full laser cycle relative to the first-cutoff harmonics. Moreover, the TAE and SAE time-frequency profiles from the longer wavelength case are much more similar, notably throughout the primary plateau. The agreement between the results from the two molecular models suggests that the recollision-enhanced HHG process is suppressed for the longer wavelength case and that HHG from the neutral molecule dominates over HHG from the cation.

3.3.2 Wavelength and intensity dependence

We now proceed to a more comprehensive analysis of the efficiency related to the rescattering mechanism behind the enhancement of HHG. To this end, we calculate HHG spectra from the A_2 TAE model for a wide range of laser parameters and evaluate the relative harmonic yields at the first and second cutoffs. In particular, the pertinent yields Y_{C1} and Y_{C2} are directly obtained from the calculated HHG spectra, based on the values of the spectral intensities at the respective cutoff harmonics. As illustrated in Fig. 3.5, we first analyze the harmonic yields at the two cutoffs for varying laser wavelengths from 1000 to 3000 nm while the peak intensity is fixed at 5×10^{13} W/cm^2. Aside from the fluctuations presumably due to channel closings [107, 108], we find that Y_{C2} decreases more drastically compared to Y_{C1} as the wavelength is increased. Overall, the scaling of the first-cutoff yield with respect to the driving wavelength is about λ^{-1}, whereas the wavelength scaling of the second-cutoff yield is about λ^{-6}. This indicates that the enhancement of HHG yield due to two-electron effects may be reduced substantially for relatively long wavelengths, specifically when the maximal return energies exceed the second ionization potential.

As we have previously discussed, the mechanism responsible for the HHG emission in the secondary plateau is an additional rescattering event by the second electron. Based on

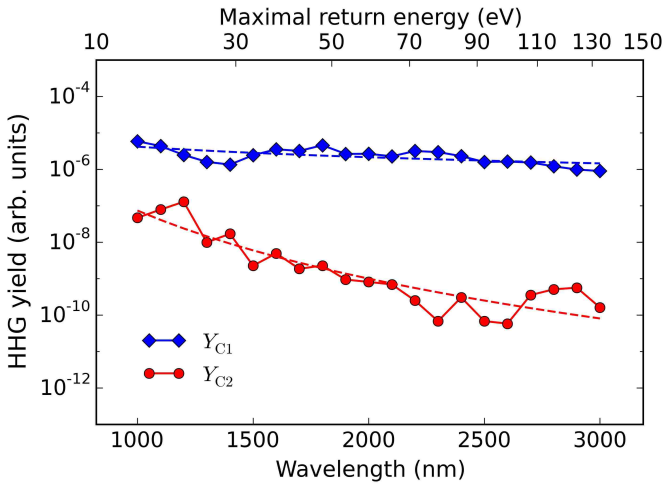

Figure 3.5: Wavelength dependence of the yields at the first and second cutoffs obtained from TAE calculations, as indicated by diamonds (Y_{C1}) and circles (Y_{C2}). The fitted trends (dashed curves) are also shown with λ^{-1} and λ^{-6} dependence for Y_{C1} and Y_{C2}, respectively. The peak intensity is fixed at 5×10^{13} W/cm^2. The scale for the corresponding maximal return energies, $3.2U_p$, is included. Reprinted with permission from [70].

this physical mechanism, we further investigate the various factors that contribute to the difference in the wavelength scalings for the first and second-cutoff yields. The rescattering mechanism following the ionization of each electron is essentially the same. We therefore expect the HHG process in the neutral molecule and the cation to have a similar wavelength scaling of λ^{-1} due to the wave packet spreading in 1D. Meanwhile, the remaining factor of λ^{-5} in the wavelength scaling of the second-cutoff yield is attributed to the recollision enhancement. In particular, this factor can be separated into two key components: (1) the electron wave packet that rescatters with the cation and (2) the inherent efficiency of the rescattering mechanism for enhancing the second ionization [109]. The former component simply gives another factor of λ^{-1} due to the wave packet spreading while the latter component, which is equal to λ^{-4}, comes from the efficiency for the ionization enhancement. Physically, this means that increasing the available electron rescattering energies results in an overall decline in the efficiency of the HHG enhancement mechanism. Based on classical NSDI studies [110], the dramatic wavelength scaling that we find can be interpreted in terms of the energy exchange between the two electrons during recollision.

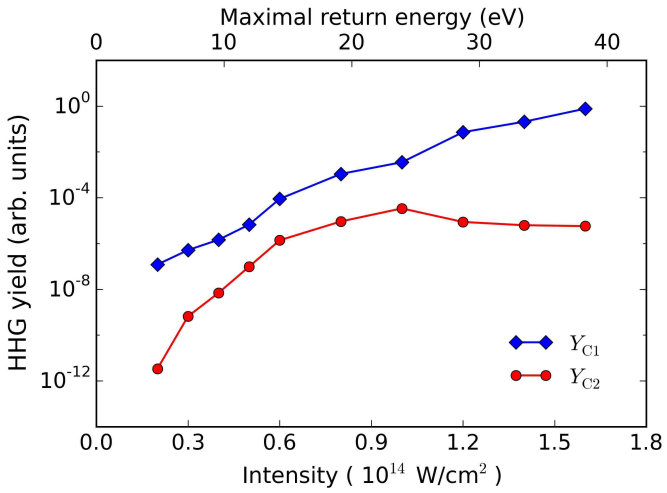

Figure 3.6: Intensity dependence of the yields at the first and second cutoffs obtained from TAE calculations, as indicated by diamonds (Y_{C1}) and circles (Y_{C2}). The laser wavelength is fixed at 900 nm. Similar to Fig. 3.5, the scale for the corresponding maximal return energies is included. Reprinted with permission from [70].

From the wavelength scaling of the second-cutoff yield, we have demonstrated that the underlying mechanism is highly sensitive to the available rescattering energies, which are determined by U_p. Additionally, we explore how the U_p scaling for increasing laser intensity affects the recollision-enhanced HHG process. For instance, a natural question is whether there is an optimal condition for the efficiency of the recollision enhancement. In Fig. 3.6, we provide the trends in the intensity dependence of the extracted yields Y_{C1} and Y_{C2} for a fixed wavelength of 900 nm. Here we consider maximal return energies that are close to the first excitation energy of A_2^+ (13.3 eV). Within an intermediate range of intensities around 0.5–1.0 $\times$ 10^{14} W/cm^2, we observe that the ratio Y_{C2}/Y_{C1} is optimal over all the intensities considered and is almost unaffected by the increase in intensity. This indicates that in general the efficiency of the recollision enhancement become relatively high for the intermediate intensities. For intensities lower than 0.5 $\times$ 10^{14} W/cm^2, the second-cutoff yields begin to drop by about 3–5 orders of magnitude below the first-cutoff yields because the associated return energies are hardly sufficient to excite the cation. Furthermore, we see that the resulting efficiency, which is evaluated by Y_{C2}/Y_{C1}, drastically decreases when the laser intensity is increased above 1.0 $\times$ 10^{14} W/cm^2. In this case, the second-cutoff

yield remains almost constant while the first-cutoff yield increases. Again, these results are consistent with the classical analysis of NSDI trends for varying laser intensities [110]. Altogether, the trends we find suggest that the efficiency for the HHG in the cation is primarily determined by the U_p scaling of the available rescattering energies. These results are consistent with our proposed recollision-driven mechanism for the enhancement of the HHG process.

Chapter 4
Time-Dependent Density Functional Theory: Part 1

As recent studies move towards more complex molecular target systems, the need to account for dynamical multielectron effects becomes apparent. In terms of HHG theory, molecular systems are more complicated compared to atomic systems because of the lower levels of symmetry. Generally speaking, the binding energies of molecular orbitals can be very close to each other such that the strong-field ionization involves multiple orbitals. Based on the shape of molecular orbitals alone, one can qualitatively predict from which valence molecular orbitals ionization is dominant, depending on the molecular alignment with respect to the laser polarization. Furthermore, molecular orbitals are in general efficiently dipole coupled to each other due to the interaction with a strong laser field. With these theoretical considerations in mind, we apply time-dependent density functional theory (TDDFT) as an *ab initio* approach to treat the interaction between a single molecular system and the driving laser field.

In principle, describing strong-field processes in molecules involves the solution of the time-dependent Schrödinger equation (TDSE) for a many-electron wave function $\Psi(t)$. However, solving the many-electron TDSE remains an impractical computational task except in the case of few electrons. As an alternative, time-dependent density functional theory provides a viable approach based on an exact formulation for solving such many-electron problems with time-dependent external fields. This approach is established from the density functional theory (DFT) formalism first proposed by Hohenberg and Kohn [111] and later extended by Kohn and Sham [112]. The generalization of DFT to time-dependent systems is demonstrated by Runge and Gross [113]. TDDFT is essentially a first-principles approach, which requires no input from experiments, for calculating pertinent properties of time-dependent systems with many electrons. Generally speaking, the (original) success of TDDFT has allowed the calculation of excited-state properties, which is a deficiency in the traditional ground-state DFT framework.

The TDDFT approach allows us to study characteristic features in HHG spectra for molecular systems, which we later compare with experimental measurements from our collaborators (see Part 2 in Chapter 5 for the results and discussion of our study). This work is mainly motivated by a large collaborative project that investigates *charge migration* in molecular systems using high harmonic spectroscopy (HHS). Charge migration refers to the ultrafast motion of a positively charged hole that is triggered by ionization or core-level excitation [114]. Molecular dynamics via ultrafast charge migration is driven by the many-electron correlation and relaxation effects, which results in the created hole moving through the molecule. Because multielectron effects in the molecular dynamics are inherently included, TDDFT provides a *direct* approach for calculating the induced single-molecule response due to a strong laser field. By direct we mean that the TDDFT approach does not rely on a factorization scheme provided by the three steps in the semiclassical model. From a theoretical perspective, we believe that this distinction is particularly important in cases where there are nontrivial effects coming from multiple molecular orbitals. In this chapter, we provide a brief introduction of the TDDFT framework and discuss the numerical details of our TDDFT calculations. Moreover, we present some properties of approximate density functionals that we think are important in HHG.

4.1 TDDFT Framework

The main idea behind TDDFT is to extract properties of a time-dependent N-electron system without directly calculating its wave function $\Psi(t)$, which depends on $3N$ spatial coordinates. Since observables of interest are often obtained from integrated quantities, the many-body problem can be significantly reduced by using functionals of the electron density

$$n(\mathbf{r},t) = N \int \Psi^*(\mathbf{r},\mathbf{r}_2,...,\mathbf{r}_N,t)\Psi(\mathbf{r},\mathbf{r}_2,...,\mathbf{r}_N,t)\, d^3\mathbf{r}_2...d^3\mathbf{r}_N, \tag{4.1}$$

which depends only on three spatial coordinates. The TDDFT formalism is based on the exact mapping between time-dependent densities and potentials [113]. In this framework,

the multielectron system is constructed in terms of a fictitious non-interacting system of Kohn-Sham (KS) orbitals $\phi_i(\mathbf{r},t)$ such that the exact density is reproduced,

$$n(\mathbf{r},t) = 2\sum_{i=1}^{N/2} |\phi_i(\mathbf{r},t)|^2 . \tag{4.2}$$

Neglecting spin degrees of freedom, we consider a (spin-restricted) system with $N/2$ doubly occupied orbitals. For our purposes we employ spin-restricted TDDFT calculations since we are mainly interested in closed-shell systems.[1] The temporal evolution of the KS orbitals is determined by a set of single-particle Schrödinger-like equations

$$i\frac{\partial}{\partial t}\phi_i(\mathbf{r},t) = \hat{H}(\mathbf{r},t)\phi_i(\mathbf{r},t) = \left[-\frac{\nabla^2}{2} + v_{\mathrm{KS}}(\mathbf{r},t)\right]\phi_i(\mathbf{r},t). \tag{4.3}$$

The KS potential $v_{\mathrm{KS}}(\mathbf{r},t)$, a functional of the density, is typically written as

$$v_{\mathrm{KS}}(\mathbf{r},t) = v_{\mathrm{KS}}[n](\mathbf{r},t) = v_{\mathrm{ext}}(\mathbf{r},t) + v_{\mathrm{H}}[n](\mathbf{r},t) + v_{\mathrm{xc}}[n](\mathbf{r},t), \tag{4.4}$$

where $v_{\mathrm{ext}}(\mathbf{r},t)$ is the external potential which includes the interaction of the electrons with the nuclei and with any applied field, $v_{\mathrm{H}}[n](\mathbf{r},t) = \int d^3\mathbf{r}' \frac{n(\mathbf{r}',t)}{|\mathbf{r}-\mathbf{r}'|}$ is the Hartree potential due to electron-electron repulsion, and $v_{\mathrm{xc}}[n](\mathbf{r},t)$ is the exchange-correlation (xc) potential which describes other nontrivial multielectron effects. The exact form of the xc potential is not known; therefore, approximate forms are in practice needed. Despite the limitation from this choice in the xc functional, TDDFT continues to be a widely used approach. The success (or failure) of TDDFT largely depends on the extensive effort dedicated to the development of new xc functionals as well as methods for extracting observables related to various applications [115].

The extension of DFT to time-dependent systems poses unique difficulties for practical calculations. In some sense, TDDFT is still a relatively new field compared to its pre-

[1] Including spin effects requires additional computational costs because the number of orbitals is doubled. Spin-unrestricted or spin-polarized (TD)DFT is typically applied to open-shell systems such as singly ionized cations of various molecules or, interestingly, the neutral O_2 molecule with a triplet ground state.

decessor (ground-state) DFT. Today most of TDDFT calculations rely on xc functionals designed for ground-state properties, i.e., apply the same xc functional from the ground-state calculation in the subsequent time propagation using an adiabatic approximation $v_{\mathrm{xc}}[n](\mathbf{r},t) = v_{\mathrm{xc}}[n(t)](\mathbf{r})$. This means that the xc potential is calculated simply from the instantaneous density. As mentioned above, one of the main problems in TDDFT comes from the inaccuracy due to approximating the xc functional, especially its lack of dependence on the history of the density (or memory dependence) [116, 117]. Functionals, which depend *explicitly* on the KS orbitals themselves, have generally been accepted to address memory effects [115, 118]. However, these orbital-dependent functionals can be computationally expensive and thus their applicability are presently limited to certain cases, depending on the "size" of the system considered. For example, the calculation of HHG spectra using TDDFT often requires large spatial grids in order to properly describe the ionized parts of the density extending far away from the atom or molecule.

4.2 Numerical Details: TDDFT Approach

4.2.1 The OCTOPUS code

OCTOPUS is an open-source software designed for the *real-time* and *real-space* implementation of TDDFT [94]. The qualifier real-time refers to explicitly solving the time evolution of the KS equations (4.3) using propagators [119]. The real-space implementation means that functions, e.g., the KS states $\phi_i(\mathbf{r},t)$ and the electron density, are represented on a spatial grid. The real-space grid representation is an alternative to established schemes used for electronic structure such as atom-centered Gaussian-type orbital (GTO) and plane-wave (PW) basis sets [120]. The main advantage of the grid-based representation is its scalability for massively parallel architectures, currently available in graphics processing units and supercomputers [121]. Particularly when considering a large spatial grid, the parallelization in OCTOPUS is carried out by separating the grid into several regions as shown in Fig. 4.1. Uniform Cartesian grids are primarily used in OCTOPUS because

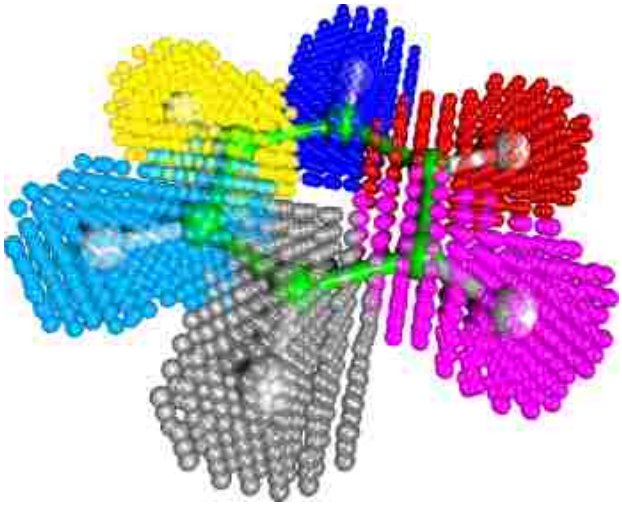

Figure 4.1: Benzene molecule represented in a grid used in OCTOPUS. With parallelization, the grid can be divided into regions (shown in different colors) that are assigned among processors. Reprinted with permission from [121].

of their simplicity; for instance, numerical derivatives can be easily obtained with finite-difference techniques [122]. More complicated discretizations can also be employed such that grids are adapted locally at the atomic core regions [123]. By reducing the distance between neighboring points in a uniform grid, the results from such real-space methods can be improved systematically within a desired accuracy. This is equivalent to adjusting the (momentum-space) cutoff energy, which is the main parameter in the PW representation.

To overcome the high resolution necessary for the core regions, real-space methods usually introduce *psuedopotentials*, which approximate the potential due to the nucleus and core electrons. The use of psuedopotentials also allows us to reduce the KS system in terms of only the valence electrons for each atom in a molecule since they are the ones that participate in chemical bonding and naturally in strong-field processes. In addition, we assume that the positions of the ions (the nuclei plus the core electrons) are fixed during the time propagation of the KS system although the ionic motion can be coupled with the electronic motion using a classical treatment [124]. From these approximations the expression for the external potential in Eq. (4.4) becomes

$$v_{\text{ext}}(\mathbf{r}, t) = v_{\text{ion}}(\mathbf{r}) + \mathbf{r} \cdot \mathbf{F}(t), \tag{4.5}$$

where the first term $v_{\text{ion}}(\mathbf{r})$ is the interaction of electrons with the ions while the second term is the interaction with the laser field.

In this work we are mainly interested in the application of TDDFT for studying HHG in molecules. Calculations of HHG spectra using the TDDFT approach have been implemented by various groups [124–126]. The calculation of the time-dependent dipole moment (or acceleration) in the TDDFT framework is straightforward, as in the single-particle TDSE framework. With the time-dependent density $n(\mathbf{r}, t)$, the induced dipole moment and dipole acceleration are expressed as

$$d(t) = \int n(\mathbf{r}, t)\, x\, d^3\mathbf{r} = 2 \sum_{i=1} \langle \phi_i(\mathbf{r}, t)|\, x\, |\phi_i(\mathbf{r}, t)\rangle \tag{4.6}$$

and

$$a(t) = -\int n(\mathbf{r}, t)\, \frac{\partial v_{\text{KS}}(\mathbf{r}, t)}{\partial x}\, d^3\mathbf{r}, \tag{4.7}$$

respectively. Here we only show the HHG component in the direction $\hat{x}$, which is chosen to be parallel to the polarization axis of the linearly polarized driving field. Note that from the composition of the density $n(\mathbf{r}, t)$ in terms of KS states (4.2), the total dipole moment can be written as the sum of contributions from individual KS states [127]. The dipole moment of each KS orbital $d_i(t) = 2\,\langle \phi_i(\mathbf{r}, t)|\, x\, |\phi_i(\mathbf{r}, t)\rangle$ comes from the solution of an effective single-particle TDSE, as indicated in Eq. (4.3). In this way the TDDFT framework provides an *ab initio* approach for the microscopic description of HHG in molecules, without the commonly used factorization imposed for the HHG spectrum. Thus, our approach does not rely on any ad hoc assumptions on which of the (valence) molecular orbitals are relevant in the collective HHG process.

4.2.2 Properties of functional approximations

Developed by Perdew and Schmidt, the *Jacob's ladder* where each class of xc functionals is represented as a rung provides a conceptual overview of density functional approximations [128]. The most simple class of xc functionals is the local density approximation

(LDA), originally derived for a homogeneous electron gas by Kohn and Sham (1965) [112]. Based on their pioneering work, most LDA functionals today apply the expression for the the exchange-correlation energy E_{xc} given by

$$E_{\mathrm{xc}}^{\mathrm{LDA}}[n] = \int n(\mathbf{r})\, \epsilon_{\mathrm{xc}}\big(n(\mathbf{r})\big)\, d^3\mathbf{r}, \tag{4.8}$$

where the exchange-correlation energy per particle $\epsilon_{\mathrm{xc}}\big(n(\mathbf{r})\big)$ is assumed to be determined by its value for a homogeneous electron gas at each point in space. The xc potential $v_{\mathrm{xc}}[n](\mathbf{r})$ is evaluated by taking the functional derivative of the xc energy E_{xc} with respect to the density, which follows from the variational principle for energy minimization provided by Hohenberg and Kohn [111]. Within this LDA framework, the KS mean field is computed from the total density including all the occupied KS states. Thus, each KS orbital experiences this mean field that also includes a contribution from itself. This is a problem in xc functionals commonly known as the *self-interaction error*. One consequence of the self-interaction error is that the KS potential has the incorrect long-range behavior mainly due to an exponential decay of v_{xc} [129]. Intuitively, the ionic and the Hartree contributions in the KS potential cancel out for a neutral system (or should decay as $-Q/r$ where $Q = 0$ is the net charge) at large distances. However, an electron ejected from the molecular binding potential does not physically interact with its own charge. This means that the xc potential, which is the last component in the KS potential, should decay as $-1/r$.

The next improvement to the xc energy is known as the generalized gradient approximation (GGA)

$$E_{\mathrm{xc}}^{\mathrm{GGA}}[n] = \int f\big(n(\mathbf{r}), \nabla n(\mathbf{r})\big)\, d^3\mathbf{r}, \tag{4.9}$$

where the information on the deviations of the density is included with a dependence on the gradient ∇n in the function $f(\cdot)$. Although the GGA is now routinely used in ground-state DFT calculations due to its applicability to a wide range of systems, it still fails in reproducing the proper asymptotic behavior of the KS mean field. Consequently,

the underestimation of ionization potentials for molecules within both the LDA and GGA is generally attributed to this lack of asymptotic Coulomb behavior. In other words, the outermost electron becomes "loosely bound" because of the self-interaction present in these xc functional approximations. This implies that addressing self-interaction errors present in (TD)DFT calculations requires xc functional schemes that are more sophisticated than the LDA or GGA. Specifically for time-dependent applications, the self-interaction error and the associated long-range behavior of the KS potential have been shown to have important implications in strong-field interactions such as ionization dynamics [130, 131].

4.2.3 Self-interaction corrections

Perdew and Zunger (PZ) proposed a scheme to remedy spurious self-interaction errors in the local approximation of the exchange-correlation energy [129]. Their work has inspired the development of a class of schemes, dubbed self-interaction corrections (SIC), which can be applied to existing local functionals. The original (PZ)SIC involves subtracting the self-interaction due to the contributions from individual orbital densities $n_i(\mathbf{r}) = |\phi_i(\mathbf{r})|^2$. This correction is applied at the energy functional level such that the combined Hartree and xc energy reads

$$E^{\mathrm{PZSIC}} = E_{\mathrm{H}}[n] + E_{\mathrm{xc}}[n] - \sum_{i=1}^{N} \left(E_{\mathrm{H}}[n_i] + E_{\mathrm{xc}}[n_i] \right) \tag{4.10}$$

As seen from this PSZIC formulation, the energy is no longer a functional of the density alone. The modified KS potential is derived in a similar manner from the variation of the SIC energy with respect to the occupied KS orbitals ϕ_i. This can lead to both practical and conceptual difficulties since the potential that is used in the effective single-particle KS equations becomes orbital-dependent.

One of the simplifications of the PZSIC scheme is based on the average density SIC (ADSIC), which has been extensively compared with other SIC schemes in Ref. [132]. Aside from returning to a mean-field potential independent of the KS state it is acting on, the

advantage of the ADSIC is that is does not require the computation of the Hartree and xc potential for each orbital. Instead, the SIC is calculated from the average density $n(\mathbf{r})/N$, replacing the contributions from each KS state in Eq. (4.10). In this way, the ADSIC assumes that the electrons in the KS system are represented by the same orbital density and therefore delocalized across the entire atom or molecule. Despite this seemingly gross simplification, the ADSIC performs very well in the calculation of ionization potentials tested for a variety of atoms and molecules (in most cases even better than PZSIC) [133]. Note that both the PZSIC and ADSIC can also be implemented to treat the densities from electronic spin states separately similar to commonly used LDA and GGA schemes. Other approaches such as splicing corrections [134, 135] and tuned range-separated hybrid (RSH) functionals [136] also recover the proper asymptotic behavior of the mean-field potential. However, because of the length and time scales we are interested in, we find that the LDA augmented with ADSIC provides the efficiency needed for our TDDFT calculations.

Chapter 5
Time-Dependent Density Functional Theory: Part 2

The process of high-order harmonic generation (HHG) offers the capability for experimental measurements to probe not only molecular structure but also ultrafast multielectron dynamics. Using the time-dependent density functional theory (TDDFT) approach, we analyze distinctive features in HHG spectra that can be linked with the electronic structure of different target molecular systems. In particular, we study structural minima found in the spectral intensity due to quantum interference effects as well as their associated spectral phase behavior. For the exchange-correlation potential, we employ the local density approximation (LDA) supplemented with the average density self-interaction correction (ADSIC). This provides an efficient way to calculate the single-molecule response in our TDDFT calculations, with the proper long-range behavior of the mean-field potential. The theoretical work presented in this chapter is motivated by the collaboration with the Agostini and DiMauro group from Ohio State University (OSU). In their experiments, the spectral intensity and phase have been fully characterized using high harmonic spectroscopy (HHS) measurements for simple linear molecules: OCS, CO_2, and N_2O. Our theoretical study serves as groundwork for first-principles modeling of the harmonic amplitude and phase measurements using HHS, which is an important technique for identifying charge migration effects in molecular systems.

5.1 Structural Minima in Molecular HHG

From the recombination step in the HHG process, the electron wave packet acts as a self-probe of the molecule from which it was ionized. The primary goal of the HHS technique is to access the recombination dipole matrix element (RDME) of the target molecule, via the coherence between the returning wave packet and the electronic bound state (see discussion in section 1.3.3). In HHS studies, prominent features in the spectral intensity and phase due to interferences in the RDME are analyzed in order to extract

information about the molecular structure or dynamics. The most simple example of a *structural* feature is the two-center minimum, which is a consequence of the destructive interference between contributions from two emitters that are spatially separated within the molecule. The appearance of pronounced (two-center) minima in HHG spectra was first demonstrated in numerical studies using TSDE for H_2 and H_2^+ model systems [137, 138]. Aside from the minimum in the spectral intensity, the two-center interference effect also has a characteristic found in the spectral phase. Note that the destructive interference can be explained in terms of a sign change in the RDME or in complex representation, the RDME goes through zero with its phase varying by π. This was also theoretically shown for the H_2 and H_2^+ model systems, wherein phase jumps of about π are found to coincide with minima in the HHG spectral intensity [137, 138].

Later experiments have verified the two-center interference effect in HHG for aligned molecules, which allows for detailed measurements in the molecular frame [139–142]. In these experimental studies [139–142], the structural minima are observed in the HHG spectra for aligned CO_2. Note that the CO_2 molecule has a highest occupied molecular orbital (HOMO) with antisymmetric combination of two $2p$ orbitals located at the O centers, as illustrated in the middle portion of Fig. 5.1. For a returning wave packet defined by the electron de Broglie wavelength $\lambda_e = 2\pi/k$, the destructive interference with an *antisymmetric* molecular orbital occurs when

$$R\cos\theta = m\lambda_e. \tag{5.1}$$

Here R is the separation distance between the two centers, θ is the angle between the molecular axis and the electron propagation direction given by the laser polarization, and m is an integer. Based on results obtained from TDSE calculations [143, 144], the *heuristic* dispersion relation $\Omega = k^2/2$ between the emitted photon energy and the electron momentum is typically used to predict the interference position in the harmonic spectrum. However, the SFA equation $\Omega = k^2/2 + I_p$ is also applicable, particularly when one considers the *asymptotic* electron momentum at large distances away from the core [145]. From Eq. (5.1) and

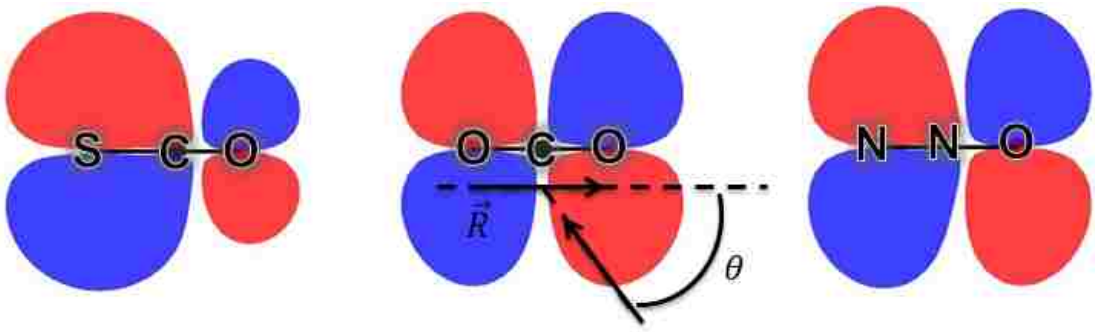

Figure 5.1: Highest occupied molecular orbitals (HOMOs) of OCS, CO_2, and N_2O (from left to right). These linear molecules have HOMOs that can be described in terms of two "centers" with p-type orbitals at either ends. In the middle, the internuclear vector $\vec{\boldsymbol{R}}$ is indicated while the rescattering angle θ for an electron wave packet is also shown with respect to the molecular axis.

the dispersion relation, we see that the structural minimum shifts to higher energies when the alignment angle θ is increased, which corresponds to a decrease in the effective distance between the two centers projected on the rescattering direction. In principle, contributions from multiple channels (or molecular orbitals) can also lead to interferences in the total recombination dipole. Nevertheless, structural minima can generally be distinguished from *dynamical* minima in experimental measurements [146, 147]. These dynamical minima rely on additional contributions from lower-lying orbitals and therefore tend to have strong sensitivity to the driving laser intensity and wavelength.

The main motivation for our collaborative study is to investigate possible effects of the recombination dipole phase differences in two-center interferences. For an extended model of HHG in aligned polar molecules [148], the condition for two-center interference can be written as

$$kR\cos\theta + \varphi_2(k,\theta) - \varphi_1(k,\theta) = (2m+1)\pi, \tag{5.2}$$

which includes additional terms for the phase difference between the two atomic centers. In the case of polar molecules, the distinction between *alignment* and *orientation* is important. Aligned molecules generally refers to some preferential direction for the molecular axis regardless of the "up" and "down" configurations, whereas a specific configuration is implied

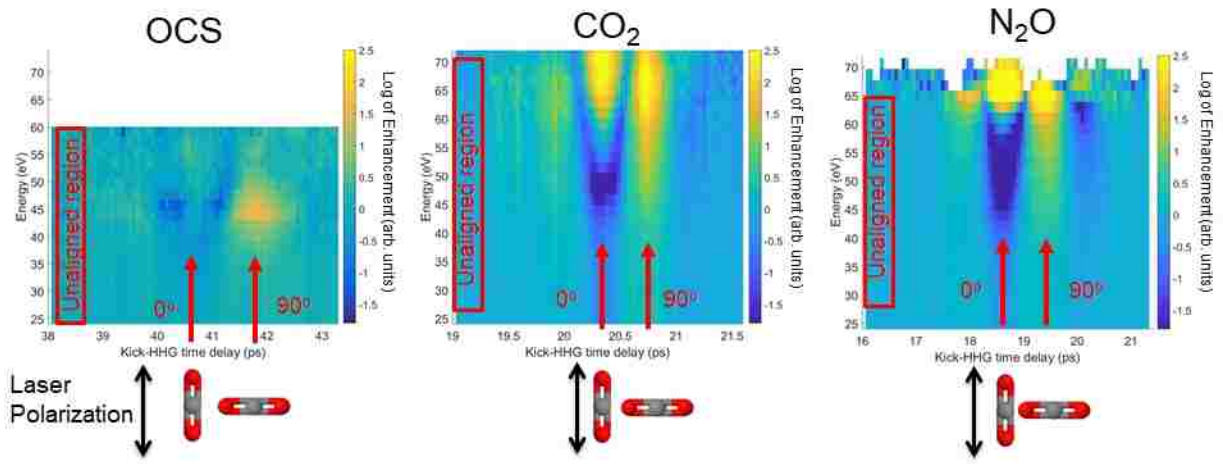

Figure 5.2: Experimental alignment dependence of HHG spectral intensity for OCS, CO_2, and N_2O (from left to right). These measurements are taken in similar HHG laser conditions, with intensity of about 1×10^{14} W/cm^2 and wavelength of 1300 nm. The alignment of the gas sample is controlled by changing the time delay between the alignment pulse and the HHG pulse, which is shown on the horizontal axes. The time delays for parallel and perpendicular alignment with respect to the laser polarization are marked by red arrows. The spectrum for each time delay is normalized to the unaligned spectrum (red boxes) to indicate the relative enhancement of the spectral intensity for varying alignment angles.

in oriented molecules. Here we will mostly consider the case with aligned molecules, such that the HHG spectrum is described in terms of the superposition of opposite molecular orientations. As a standard technique for experimental studies, the molecular alignment is achieved using an initial laser pulse, which creates a coherent superposition of rotational states in the molecule [149, 150]. The induced rotational wave packet provides high degrees of molecular alignment at regular time intervals which are associated with the rotational revivals. This means that, in experiments, HHG for aligned molecules can be studied by applying a generating pulse at various time delays after the aligning pulse.

As the motivation for our theoretical study, we present some of the experimental results from the OSU measurements. In Fig. 5.2, the alignment dependence of the HHG spectral intensity are shown for three molecules: OCS, CO_2, and N_2O. Notice that specific time delays between the alignment pulse and the HHG pulse are assigned to molecular alignment angles from 0° to 90° (red arrows). From the middle and right panels of Fig. 5.2, we

see that there is a clear minimum that starts from 0° for both CO_2 ($\approx$ 48 eV) and N_2O ($\approx$ 50 eV) and then shifts to higher energies as the alignment angle increases to intermediate angles. This is a signature of the two-center interference effect. The quite similar behavior of the alignment-dependent HHG yield in CO_2 and N_2O can be explained by the structure of their HOMOs, which are depicted in the middle and right portions of Fig. 5.1. Even though N_2O is polar unlike CO_2, these two molecules are isoelectronic and have similar separation distances between the terminal atoms. Compared to CO_2 and N_2O, the results for the harmonic spectral intensity in OCS (left panel of Fig. 5.2) show a different alignment-dependent profile of the minimum. Specifically, the deepest minimum in the spectral intensity for OCS is found around 30–40° alignment ($\approx$ 48 eV) while the minimum for the 0° alignment is rather faint. Although OCS has a HOMO with two centers (shown in left portion of Fig. 5.1) similar to CO_2, the substitution of S (instead of O) results in a $3p$ orbital (instead of $2p$ orbital) centered at one of the terminal atoms. Hence, the difference in the experimental measurements of the alignment-dependent harmonic yields for CO_2 and OCS indicate that the HHS technique has the sensitivity to probe structural features specific to the target molecule in the aligned sample. In what follows we discuss the results of our HHG calculations using the TDDFT approach and the post-processing analysis that we apply to the HHG signal for extracting harmonic amplitudes and phases.

5.2 Molecular HHG: TDDFT Approach

Based on the numerical methods detailed in the previous chapter (4), we solve the time-dependent Kohn-Sham (KS) equations (4.3) to model the multielectron dynamics in single-molecule systems interacting with a strong infrared (IR) field. In our calculations, we focus on the HHG emission from molecular target systems, CO_2 and OCS, which we compare with the experimental measurements. The exchange-correlation potential is approximated using the LDA, including the Perdew-Zunger formulation for the correlation functional [129]. Since the LDA is generally known to have self-interaction errors, we implement the LDA

augmented with the ADSIC [132], which gives the proper long-range decay $(-1/r)$ of the KS potential. This generally results in an improved ionization potential, determined by the energy of the highest occupied molecular orbital, $I_p = -E_{\mathrm{HOMO}}$. Applying fixed molecular geometry, we set the bond lengths similar to their experimental values: $R_{\mathrm{CO}} =$ 1.16 Å for CO_2, $R_{\mathrm{CO}} = 1.15$ Å and $R_{\mathrm{CS}} = 1.56$ Å for OCS. We assume that only the 16 outermost electrons (with 8 corresponding active orbitals) participate in the dynamical response. The electron-ion interactions $[v_{\mathrm{ion}}(\mathbf{r})]$ are represented by the nonlocal Kleinman-Bylander form [151] of the norm-conserving Troullier-Martins pseudopotentials [152]. The ground-state properties are obtained from the self-consistent solution of the (field-free) KS equations, checking for the convergence in both the densities and the orbital energies from successive iterations. The computed values for the ionization potentials are 14.5 eV for CO_2 and 11.7 eV for OCS, which are in good agreement with their respective experimental values, 13.8 eV and 11.2 eV [153].

Initialized from the ground state of the molecular system, the time-dependent KS equations are propagated with an applied laser field. In this study the envelope for the linearly polarized laser field has a similar form given by Eq. (3.6), which ramps up during the first two cycles and remains constant afterwards. This "flat-top" pulse allows a straightforward comparison with the SFA analysis for a well-defined peak intensity during the half-cycles after the field ramp-up. Because of the long driving wavelengths that we consider (1300–1500 nm), we used a spatial grid that accounts for the ionized parts of the density extending far away from the molecule. The extent of the uniform Cartesian grid is taken to be $|x| \leq 195$ a.u. and $|y| = |z| \leq 30$ a.u. For alignment-dependent calculations, the molecular axis is varied such that the plane of rotation is the xy-plane while the laser polarization is fixed along the x-axis. Thus, we define the molecular alignment angle θ relative to the $+x$-axis. The grid spacing is set as 0.4 a.u. and the propagation time step as 0.05 a.u. We ensure the convergence of our calculations with respect to the discretization of the numerical grid, e.g., by checking against results obtained using a smaller grid spacing

or time step. We also apply an optimized complex absorbing potential near the edges of the spatial grid to prevent spurious reflections.

5.2.1 Seeded HHG using attosecond pulse train

From the theoretical side, it is important to characterize the molecular HHG emission preferably at the sub-cycle level in order to extract information about the molecular structure and the induced ultrafast dynamics. This can be a challenging task since the harmonic signal obtained from numerical methods consists of contributions from multiple quantum paths, which interfere in the spectral domain. In experiments, the different phase matching properties of these quantum path contributions can be harnessed so that they can be preferentially selected or spatially separated in the far field (see discussion of macroscopic effects in section 1.4). However, macroscopic calculations of HHG typically require several hundred single-molecule calculations and are therefore not currently feasible for systematic studies of charge migration effects exhibited in harmonic spectra. In this work we calculate the single-molecule response in the presence of two fields: (1) a strong IR field and (2) an attosecond pulse train (APT) composed of several odd harmonics of the IR field. The objective of the seeded HHG using APT is to launch the electron wave packet on the short trajectory upon ionization, thereby obtaining clean spectra wherein the short trajectory contribution is preferentially selected. When the time delay between the IR and the APT pulses is appropriately chosen, the two-pulse scheme has been theoretically and experimentally demonstrated to generate harmonic spectra that are dominated by the short trajectory contribution [154–156].

In our TDDFT calculations, the total field with polarization along the x-direction is expressed as

$$F(t) = F_0 f(t) \sin(\omega t) + F_1 f(t) \sum_q \sin(q\omega[t - t_d]), \tag{5.3}$$

where the peak intensities for the IR and the APT fields are tuned by the amplitudes F_0 and F_1, respectively. The field envelope $f(t)$ given by Eq. (3.6) is set to be the same for

both fields. Each of the short bursts in the APT is naturally synchronized with the IR field and the sub-cycle delay between the IR and the APT fields is controlled by parameter t_d. Five consecutive odd harmonics are chosen such that the central harmonic is close to the ionization threshold. Since there are no relative phases introduced in the odd harmonics, each burst in the APT is Fourier-transform limited. In these seeded HHG calculations, the APT peak intensity needs to be high enough in order to substantially enhance the HHG yield from the short trajectory, i.e., to enhance the ionization yield at the correct release time. Nevertheless, we also keep the APT intensity relatively low compared to the IR intensity in order to reduce excitations coming from lower-lying orbitals due to the APT (which is not present in the experiment). For relatively weak APT intensities about 1–3% of the IR intensity, our results are in general robust except for an overall enhancement of the harmonic yield that is roughly linear with the APT intensity.

We first consider the case of aligned CO_2 with parallel molecular configuration relative to the driving field polarization. For the IR field, we apply laser parameters similar to the experiment, with the peak intensity equal to 8×10^{13} W/cm^2 and the wavelength equal to 1300 nm. The APT field is composed of five odd harmonics of the IR field (H7–15) and has a peak intensity that is 2% of the IR intensity. As seen from the Gabor time-frequency analysis in the left panel of Fig. 5.3, the resulting HHG emission has contribution from the short trajectory which is significantly enhanced. This is achieved by tuning the time delay t_d between the IR and the APT fields, which essentially controls the time at which the electron wave packet is released into the continuum during the IR laser cycle. The subsequent dynamics of the initiated wave packet can then be driven by the strong IR field. From this enhancement process, the properties of the short trajectory contribution is therefore mostly determined by the IR field (independent of the APT field). In our study we mainly present results for an optimized delay of $t_d = -0.17$ laser cycle for the short trajectory contribution. Here the negative sign in the time delay means that the APT field comes *before* the zero crossing of the IR field.

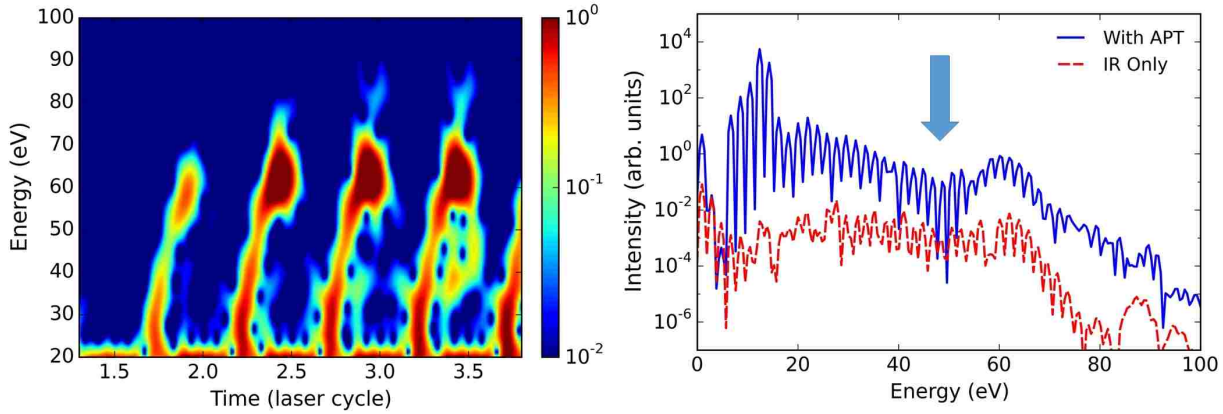

Figure 5.3: The left panel shows the time-frequency profile of the seeded HHG in aligned CO_2 ($\theta = 0°$) using an IR field and an APT field. For the time-frequency analysis, a Gabor transform is applied as indicated in Eq. (3.9). The IR field has a peak intensity of 8×10^{13} W/cm^2 and a wavelength of 1300 nm. The APT field is constructed from odd harmonics of the IR field (H7–15) and its intensity is set to 2% of the IR intensity. The time delay between the IR and the APT fields is optimized such that the harmonic yield is mostly from the short trajectory contribution. In the right panel, a prominent minimum is seen from the corresponding HHG spectrum for the IR+APT case (solid blue). For reference, the HHG spectrum for the IR only case is also shown (dashed red). The harmonic spectra are obtained by taking the Fourier transform of the dipole acceleration for the duration of 1.5–3.5 laser cycles.

From the Gabor analysis in Fig. 5.3, we find that the harmonic signal is mostly similar for the subsequent half-cycles after the field ramp-up at $t = 2$ laser cycles, except for the additional quantum path contributions that appear in later half-cycles. The associated HHG spectrum taken from the first few half-cycles after the field ramp-up (solid blue) is shown in the right panel of Fig. 5.3. A clear minimum is found in the HHG spectrum for the case with the APT field. The position of the minimum is close to where one would expect the two-center interference effect to occur, which is a good indication that the seeded HHG process is a sensitive probe of the molecular structure of CO_2. In addition, notice that the enhancement of the ionization due to the APT results in an overall HHG signal that is much higher than the IR only case (dashed red). Since we are interested in extracting the harmonic spectral amplitudes and phases, it is crucial that the short trajectory contribution due to enhancement from the APT field is substantially higher than the "noise level" given by the HHG signal from the IR only case.

For various alignment angles, we calculate the HHG spectra from both CO_2 and OCS molecular targets. To ensure that the ionization due the IR field alone is kept very low, we adjust the IR field parameters to peak intensity equal to 6×10^{13} W/cm^2 and wavelength equal to 1500 nm. These laser parameters are chosen such that the cutoff energy is about same as the HHG spectrum in Fig. 5.3 but with much lower ionization from the IR field alone. The overall noise level in the signal is therefore significantly reduced for the seeded HHG calculations compared to the 1300 nm case. In our analysis, we check whether the signal from the seeded HHG is sufficiently high relative to the HHG signal when only the IR field is present. As labeled in each panel of Fig. 5.4, we display the Gabor profiles of the emitted harmonics from CO_2 and OCS for alignment angles 15° and 45°. Here we only

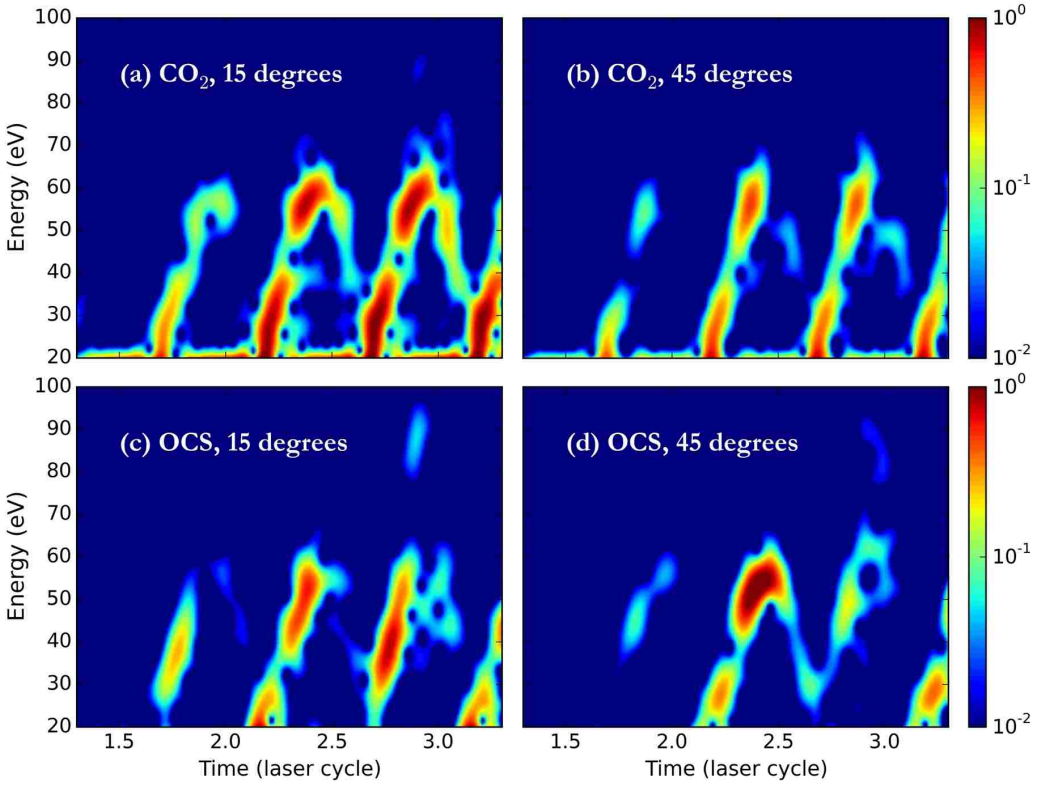

Figure 5.4: Gabor analysis of the HHG emission along the x-direction in aligned CO_2 (upper panels) and oriented OCS (lower panels) single molecules. For each molecular system, we show two alignment angles that are defined relative to the laser polarization ($+x$-axis). The IR field has a peak intensity equal to 6×10^{13} W/cm^2 and a wavelength equal to 1500 nm. The applied APT fields are composed of harmonics 9–17 with 2% of the IR intensity for CO_2 and harmonics 7–15 with 1% of the IR intensity for OCS. In all cases, the delay of the APT field is set to 0.17 laser cycle before the zero crossing of the IR field, as in Fig. 5.3.

consider the harmonic signal parallel to the laser polarization. These time-frequency profiles confirm that in general the HHG signal is dominated by the short trajectory contribution, regardless of the molecular target or the alignment angle.

By comparing the time-frequency profiles for CO_2 and OCS in Fig. 5.4, we observe striking differences in the sub-cycle HHG emission for OCS during the first two half-cycles after the ramp-up. Each alternating half-cycle corresponds to ionization from and recombination to either side of the polar OCS molecule. The returning wave packet rescatters with a different orientation of the molecule and thus a different photorecombination process occurs every half-cycle of the IR field. In principle, the HHG signal for the two orientations need to be coherently added in order to compare with the experiment, where the target system is an aligned molecular sample. We note that, in the case of alignment angle $\theta = 45^\circ$ (lower right panel), we find that the HHG signal from the first half-cycle after the field ramp-up dominate over the signal from the next half-cycle. This variation in the strengths of the harmonic signal in two consecutive half-cycles can be attributed to a strong preference in the ionization for one molecular orientation over the other.

5.2.2 Sub-cycle analysis of the HHG signal

So far our TDDFT calculations indicate that the HHG seeding with an APT field provides a viable tool for preferentially enhancing the short trajectory contribution in the harmonic signal. Next we proceed to the discussion of the numerical techniques that we utilize for the post-processing analysis of the HHG signal at the sub-cycle level. The primary goal of this post-processing analysis is to analyze pertinent features in the harmonic spectral amplitudes and phases, which are associated with the electronic structure of the target molecule. The left panel of Fig. 5.5 shows a typical time-dependent dipole acceleration signal (red curve), which is dominated by large below-threshold oscillations. This makes a direct time-frequency analysis of the harmonic signal rather problematic. As an alternative, we implement the following procedure: (1) filtering out the low-frequency components from the raw signal during specific half-cycles of the IR field and (2) taking a windowed Fourier

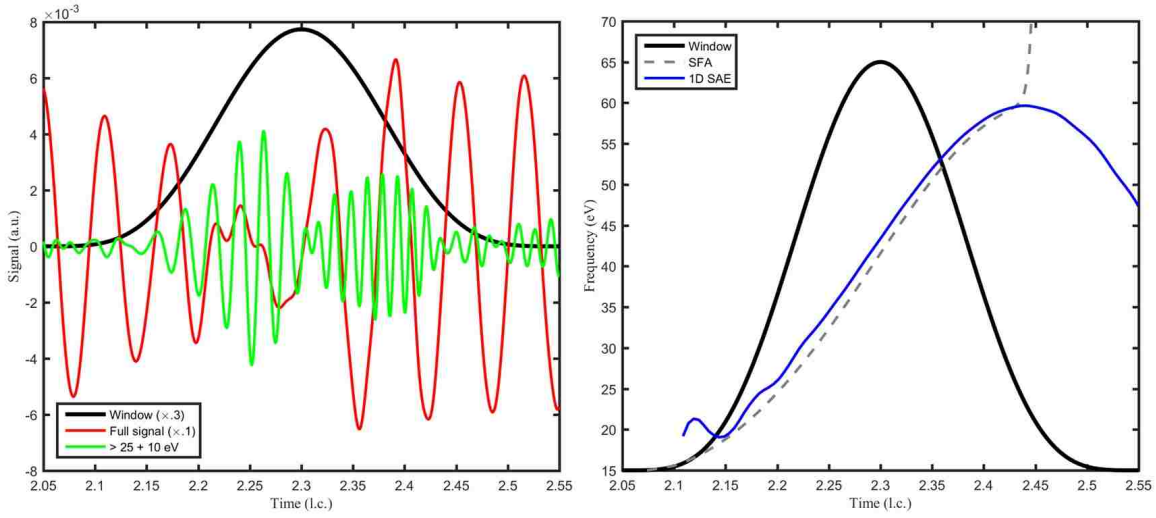

Figure 5.5: Processing of the HHG signal. Left panel: A typical dipole acceleration signal obtained from seeded HHG calculations using TDDFT (red curve). The high-frequency signal (green curve) is acquired from the full signal by filtering out the frequency components below 25 eV, with a 10-eV smooth transition. A $\cos^4$ window used to select the short trajectory contribution is also shown (black curve). Right panel: Time-frequency map from SFA analysis (dashed gray curve) with matching parameters for the ionization potential and the laser intensity and wavelength. Time-frequency map from a reference 1D SAE calculation with the same matching parameters (blue curve). As in the left panel, the $\cos^4$ window used for the short trajectory contribution is similarly shown (black curve).

transform of the filtered signal to select the short trajectory contribution. We restrict our analysis to the first few half-cycles after the field ramp-up since they are relatively "clean" compared to the later half-cycles when additional quantum path contributions start to appear (see for instance the left panel of Fig. 5.3).

The procedure for the post-processing analysis is illustrated in Fig. 5.5. In the left panel, we display the filtered signal (green curve), which is acquired by filtering out the Fourier components below 25 eV and taking the Fourier transform back to the time domain. Because of the APT introduced in the TDDFT calculations, this filtered signal is already observed to have characteristics that reflect contribution from the short trajectory. For instance, the frequency of the oscillations increases over time within the duration of a laser half-cycle. We also find a minimum in the overall envelope of the filtered HHG signal at about $t = 2.3$ laser cycles, which is consistent with the minimum in the harmonic spectral

intensity. To further isolate the short trajectory contribution, we apply a $\cos^4$ window to the filtered signal over the duration 0.05–0.55 laser cycles, from the beginning of a given half-cycle (see both panels of Fig. 5.5). For the sub-cycle analysis, we analyze the *total* harmonic yield in CO_2 for different alignment angles. We note that there can be substantial contributions in the total harmonic yield coming the HHG signal along the y-direction, particularly when the molecular axis is not perfectly parallel or perpendicular to the laser polarization. As previously demonstrated in numerical studies of the two-center effect in H_2^+, the harmonic signal perpendicular to the driving field can sometimes obscure the appearance of the interference minimum [157]. We therefore take the total HHG yield to be the sum of contributions along the x- and y-directions, $|\mathcal{S}_x(\Omega)|^2 + |\mathcal{S}_y(\Omega)|^2$.

To test the accuracy of our methods, we follow the two-center interference minimum in the total HHG yield as the molecular axis is rotated relative to the laser polarization. In the left panel of Fig. 5.6, the alignment-dependent spectral intensities in CO_2 show that the positions of actual minima (open circles) generally move to higher energies as the alignment angle is increased. Except for some alignment angles, we see that the minima in the HHG yield are consistent with the geometric expectation for the position of a two-center interference minimum, i.e., with a $1/\cos^2\theta$ dependence (dashed white curve). We attribute the discrepancies between our TDDFT results and the geometric expectation to possible shifts in the positions of the interference minima caused by the APT field. By analyzing the individual orbital contributions to the harmonic yield (not shown here), we have found that inner KS orbitals below the degenerate HOMOs can also have a strong response to the APT field. For consistency, we also give the alignment-dependent harmonic yields from OCS in the right panel of Fig. 5.6. Similarly, we find an overall good agreement between the observed minima from the calculated harmonic yields and the geometric expectation.

Besides the minimum found in the harmonic spectral intensity, the two-center interference effect is also associated with a variation in the spectral phase [137, 138, 141]. Within the QRS framework (see discussion in section 1.3.3), the spectral phase is generally known

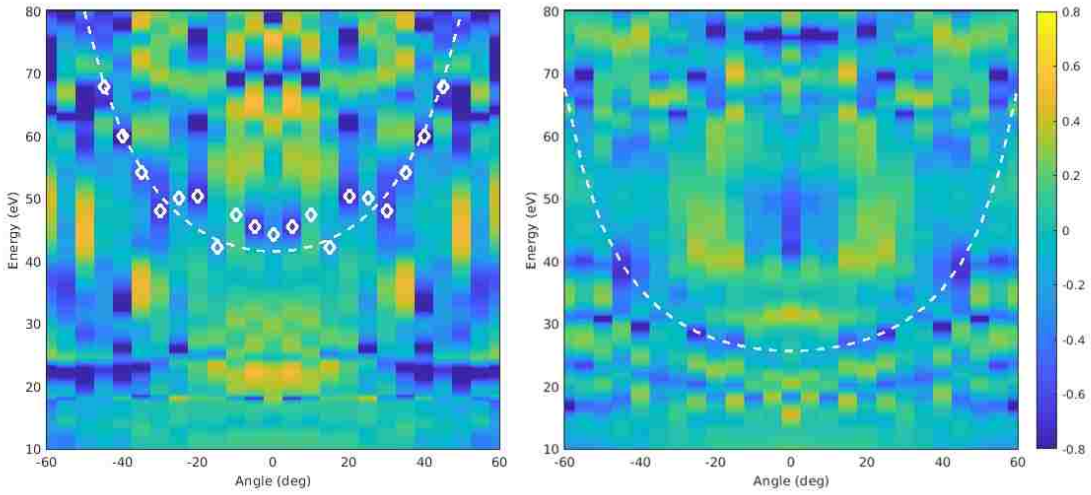

Figure 5.6: Alignment-dependent harmonic spectral yields in CO_2 (left panel) and OCS (right panel). These are extracted from the time signal during the first half-cycle after the field ramp-up for CO_2 and from the averaged time signal during the first two half-cycles after the field ramp-up for OCS. The plot is shown in $\log_{10}$ scale and the spectral intensity for each harmonic energy is normalized by the angle-averaged value. Actual positions of minima from the spectral intensity are indicated by open circles in the left panel. The dashed curve in the each panel is shown as a guide for the eye and is given by a $1/\cos^2\theta$ dependence, which is the geometric expectation for two-center interference minima at varying alignment angles.

to have two contributions: (1) from the rescattering electron wave packet and (2) from the RDME which is the one we are interested in. The first contribution is directly related to the *attochirp*, which have been experimentally measured in Ref. [158]. Based from the semiclassical model of HHG, the attochirp is attributed to the monotonic increase in the emission time with harmonic order for the short trajectory. By carefully removing this contribution (1), features in the phase variation that are specific to the molecular target can therefore be analyzed. In addition to the filtered short-trajectory signal, we calculate the corresponding time-frequency map from two methods, namely the SFA model and the numerical solution of the SAE-TDSE for a 1D soft-Coulomb atom. For both methods we match the parameters from our TDDFT calculations, such as the ionization potential and the laser intensity and wavelength. As exhibited in the right panel of Fig. 5.5, there is a systematic shift to earlier emission times in the 1D SAE model compared to the SFA

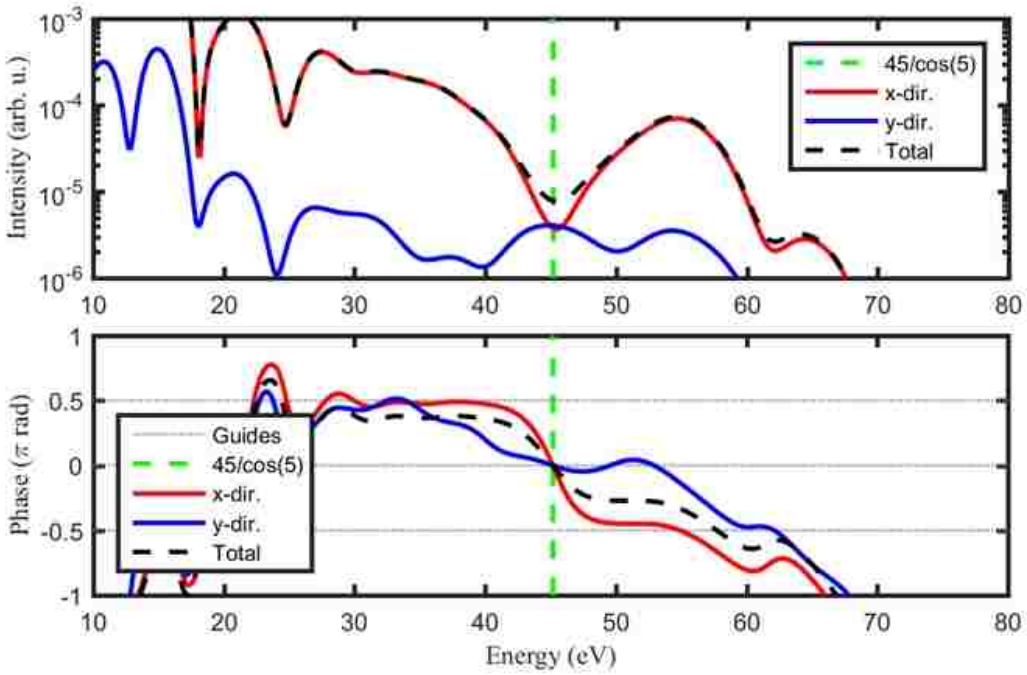

Figure 5.7: Extraction of the harmonic spectral intensity and target-specific phase for CO_2 at alignment angle $\theta = 5°$. In both panels, the spectral intensity and its associated phase (dashed black curves) are obtained from the total HHG signal, which include contributions from the signal along the x- and y-directions (red and blue curves). The target-specific phase shown in the lower panel has been corrected by subtracting the generic phase from an atomic reference signal (see text). The vertical dashed lines indicate the position of the two-center interference minimum.

model. In general, we find that the 1D SAE model gives a more accurate description of the time-frequency map for the short trajectory. Hence, we use the calculated signal from the 1D SAE model as a reference for the extraction of the target-specific phase.

To exemplify the "full" extraction procedure using the windowed Fourier transform, the acquired spectral intensity (upper panel) and target-specific phase (lower panel) in CO_2 at alignment angle $\theta = 5°$ are shown in Fig. 5.7. In both panels we provide the results from the total HHG signal (dashed blacks) which includes contributions from the signal along the x- and y-directions. For our purposes we are only interested in the phase variation, rather than the actual values. The target-specific phase contribution shown in the lower panel has been corrected by subtracting the generic phase contribution for the reference signal, which is calculated from the 1D SAE atomic model. Consistent with a two-center interference

effect, we observe from the lower panel of Fig. 5.7 that a near-π phase jump is recovered in the HHG signal parallel to the laser polarization (red curve). Notice that the shift in the spectral phase coincides with the position of the minimum in the spectral intensity (vertical dashed lines). Interestingly, we find that the contribution from the perpendicular HHG signal (blue curve) can modify the phase behavior of the total HHG signal near the minimum, i.e., resulting in a slightly lower phase jump. This means that including the HHG contribution from the perpendicular direction is important for analyzing the spectral phase near the interference minimum. We have found reasonable agreement with experimental measurements of the harmonic spectral phase, but only for small alignment angles in CO_2. In this thesis, we are not showing any of the systematic calculations of the spectral phase or any of the experimental phase measurements. Understandably, it is much harder to extract the angle-dependent spectral phase from the numerically obtained HHG signal compared to the spectral yield. In this regard, we will examine how the APT field itself may affect the extraction of both the spectral intensity and phase.[1]

5.3 Future Work

In conclusion, we are working closely with our collaborators from OSU in the analysis and interpretation of their experimental results. From the theoretical side, our results indicate that first-principles calculations using TDDFT provide a feasible approach for extracting harmonic spectral amplitudes and phases, which can be compared directly with experimental HHS measurements. To further improve our procedure, refinements can be made in the calculation of the single-molecule harmonic signal within the TDDFT framework as well as in the time-frequency analysis of the harmonic signal. For future studies, we are also interested in investigating the control of charge migration via its dependence on the molecular alignment and how pertinent dynamical features are manifested in HHS measurements. Additionally, the evolution of such dynamical features in the HHG spectrum

[1]From a different perspective, the APT or an isolated XUV pulse can also be used to potentially initiate the ultrafast electron dynamics within the molecule (see for instance [159, 160]).

with respect to changes in the laser parameters such as the peak intensity and wavelength will be explored.

Chapter 6
Summary and Outlook

In this thesis we report theoretical studies using (semi)classical and quantum approaches, which we utilize to examine the HHG process in a variety of systems and models. The properties of the emitted extreme-ultraviolet (XUV) light via HHG naturally contains information about the ultrafast electron dynamics driven by a strong infrared (IR) laser field. In Chapter 2, we have discussed the first approach based on classical trajectory Monte Carlo (CTMC), wherein an ensemble of independent classical electron trajectories is propagated in the presence of an atomic argon potential and the IR driving field with elliptical polarization. Recolliding trajectories, which are initially ionized from the atomic core and subsequently driven back by the laser field, are assumed to contribute to the HHG process. Within this recollision model of HHG, we demonstrate that the inclusion of the atomic potential can give rise to a rich and complex recollision dynamics. This goes beyond the commonly used strong field approximation, where the atomic potential is ignored during the propagation dynamics. Moreover, our nonlinear dynamical analysis reveals that the behavior of these returning trajectories is regulated by a set of recolliding periodic orbits that survive even at relatively high ellipticity. Notably, these RPOs provide a way for the low-energy long trajectories to return to the ionic core with the aid of the atomic potential, which explains their persistence with increasing laser ellipticity.

Next we shift to quantum approaches that we employ in order to model the HHG process in multielectron molecular systems. In Chapter 3, we have presented a theoretical investigation of dynamical multielectron effects that can lead to the enhancement of molecular HHG emission. Using a model molecular system (A_2), we numerically solve the time-dependent Schrödinger equation (TDSE) with two active electrons, each restricted to one dimension. Our results show that even at intensities well below the single ionization saturation, harmonics generated from the cation (A_2^+) is significantly enhanced due to the rescattering of the electron that is initially ionized. This two-electron effect is observed from

the appearance of secondary plateaus and cutoffs in the calculated HHG spectra, thereby extending beyond the predicted cutoff from the single active electron (SAE) approximation. In addition, the time-frequency analysis of the calculated HHG signals confirms a delayed mechanism for the emission of the second-cutoff harmonics relative to the first-cutoff harmonics. Based on the laser intensity and wavelength dependence of the relative second-cutoff HHG yields, we provide an interpretation of the inherent efficiency of the recollision-enhanced HHG process in terms of the available rescattering energies.

Finally, in Chapters 4 and 5, we explore the HHG process in more realistic molecular systems using the real-space numerical grid implementation of the time-dependent density functional theory (TDDFT). Here the TDDFT framework provides a mean-field approach for describing the strong-field dynamics in simple molecular systems with multiple active orbitals. In our single-molecule TDDFT calculations, we include a weak attosecond pulse train (APT) constructed from a few odd harmonics of the linearly polarized IR driving field. As determined by the delay between the IR and the APT fields, the ionization time for the initiated electron wave packet can be chosen such that the short trajectory contribution is preferentially enhanced. Additionally, we have developed numerical techniques for the post-processing analysis of the HHG signal obtained from the TDDFT calculations. Overall, this scheme allows for a direct comparison with experimental alignment-dependent measurements of the harmonic spectral intensity and phase. From our benchmark calculations in CO_2 and OCS, we demonstrate the applicability of our approach for studying structural features in harmonic spectra generated from molecules aligned at different angles relative to the laser polarization. The characterization of these pertinent features provide insight towards systematic studies of correlation-driven dynamical effects in molecules.

To conclude, we expect high harmonic spectroscopy (HHS) to continue as an important technique in future studies for characterizing attosecond charge migration dynamics in increasingly complex molecules. In experiments, the molecular alignment or orientation will remain to be the primary limitation for accessing the recombination dipole matrix element

(RDME) in these target systems. From the theoretical perspective, continuous efforts will also be required in order to develop numerical and analytical models that will help interpret the experimental measurements of harmonic spectral amplitudes and phases. Since TDDFT provides an "all-at-once" (or top-down) approach for calculating HHG spectra in molecular systems, we believe that it will be advantageous to use TDDFT for studying charge migration in large molecules particularly in cases with many participating molecular orbitals. This is in stark contrast with factorization (or bottom-up) schemes for HHS, where individual contributions are essentially treated as SAE channels. Nevertheless, the combination of both top-down and bottom-up approaches can potentially address which signatures of charge migration are relevant in molecular HHG. Aside from the electron dynamics, it will also be interesting to investigate the coupled electron-nuclear dynamics and determine how the ultrafast electron motion within molecules can play a decisive role in the longer time scale processes, e.g., dissociative ionization.

References

[1] A. McPherson, G. Gibson, H. Jara, U. Johann, T. S. Luk, I. A. McIntyre, K. Boyer, and C. K. Rhodes, J. Opt. Soc. Am. B **4**, 595 (1987).

[2] M. Ferray, A. L'Huillier, X. F. Li, L. A. Lompre, G. Mainfray, and C. Manus, J. Phys. B: At. Mol. Opt. Phys. **21**, L31 (1988).

[3] E. Goulielmakis, Z.-H. Loh, A. Wirth, R. Santra, N. Rohringer, V. S. Yakovlev, S. Zherebtsov, T. Pfeifer, A. M. Azzeer, M. F. Kling, et al., Nature **466**, 739 (2010).

[4] H. Wang, M. Chini, S. Chen, C.-H. Zhang, F. He, Y. Cheng, Y. Wu, U. Thumm, and Z. Chang, Phys. Rev. Lett. **105**, 143002 (2010).

[5] M. Hentschel, R. Kienberger, C. Spielmann, G. A. Reider, N. Milosevic, T. Brabec, P. Corkum, U. Heinzmann, M. Drescher, and F. Krausz, Nature **414**, 509 (2001).

[6] P. M. Paul, E. S. Toma, P. Breger, G. Mullot, F. Augé, P. Balcou, H. G. Muller, and P. Agostini, Science **292**, 1689 (2001).

[7] J. Li, X. Ren, Y. Yin, K. Zhao, A. Chew, Y. Cheng, E. Cunningham, Y. Wang, S. Hu, Y. Wu, et al., Nature Commun. **8**, 186 (2017).

[8] T. Gaumnitz, A. Jain, Y. Pertot, M. Huppert, I. Jordan, F. Ardana-Lamas, and H. J. Wörner, Optics Express **25**, 27506 (2017).

[9] P. B. Corkum and F. Krausz, Nature Phys. **3**, 381 (2007).

[10] F. Calegari, G. Sansone, S. Stagira, C. Vozzi, and M. Nisoli, J. Phys. B: At. Mol. Opt. Phys. **49**, 062001 (2016).

[11] M. F. Ciappina, J. A. Pérez-Hernández, A. S. Landsman, W. A. Okell, S. Zherebtsov, B. Förg, J. Schötz, L. Seiffert, T. Fennel, T. Shaaran, et al., Rep. Prog. Phys. **80**, 054401 (2017).

[12] Y. Mairesse, J. Higuet, N. Dudovich, D. Shafir, B. Fabre, E. Mével, E. Constant, S. Patchkovskii, Z. Walters, M. Y. Ivanov, et al., Phys. Rev. Lett. **104**, 213601 (2010).

[13] A. D. Shiner, B. E. Schmidt, C. Trallero-Herrero, H. J. Wörner, S. Patchkovskii, P. B. Corkum, J. C. Kieffer, F. Légaré, and D. M. Villeneuve, Nature Phys. **7**, 464 (2011).

[14] P. M. Kraus, B. Mignolet, D. Baykusheva, A. Rupenyan, L. Hornỳ, E. F. Penka, G. Grassi, O. I. Tolstikhin, J. Schneider, F. Jensen, et al., Science **350**, 790 (2015).

[15] F. Krausz and M. Ivanov, Rev. Mod. Phys. **81**, 163 (2009).

[16] A. H. Zewail, J. Phys. Chem. A **104**, 5660 (2000).

[17] K. J. Schafer, B. Yang, L. F. DiMauro, and K. C. Kulander, Phys. Rev. Lett. **70**, 1599 (1993).

[18] P. B. Corkum, Phys. Rev. Lett. **71**, 1994 (1993).

[19] P. Salières, B. Carré, L. Le Déroff, F. Grasbon, G. Paulus, H. Walther, R. Kopold, W. Becker, D. Milošević, A. Sanpera, et al., Science **292**, 902 (2001).

[20] M. Lewenstein, P. Balcou, M. Y. Ivanov, A. L'Huillier, and P. B. Corkum, Phys. Rev. A **49**, 2117 (1994).

[21] L. V. Keldysh, Zh. Eksp. Teor. Fiz. **47**, 1945 (1964), Sov. Phys. JETP **20**, 1307 (1965).

[22] A. M. Perelomov, V. S. Popov, and M. V. Terentev, Sov. Phys. JETP **50**, 1393 (1966).

[23] M. V. Ammosov, N. B. Delone, and V. P. Krainov, Sov. Phys. JETP **64**, 1191 (1986).

[24] A. S. Landsman and U. Keller, J. Phys. B: At. Mol. Opt. Phys. **47**, 204024 (2014).

[25] X. M. Tong, Z. X. Zhao, and C. D. Lin, Phys. Rev. A **66**, 033402 (2002).

[26] O. I. Tolstikhin, T. Morishita, and L. B. Madsen, Phys. Rev. A **84**, 053423 (2011).

[27] A.-T. Le, X.-M. Tong, and C. D. Lin, Phys. Rev. A **73**, 041402 (2006).

[28] M. Lewenstein, P. Salières, and A. L'Huillier, Phys. Rev. A **52**, 4747 (1995).

[29] J. Itatani, J. Levesque, D. Zeidler, H. Niikura, H. Pépin, J.-C. Kieffer, P. B. Corkum, and D. M. Villeneuve, Nature **432**, 867 (2004).

[30] O. Smirnova, Y. Mairesse, S. Patchkovskii, N. Dudovich, D. Villeneuve, P. Corkum, and M. Y. Ivanov, Nature **460**, 972 (2009).

[31] A.-T. Le, R. R. Lucchese, S. Tonzani, T. Morishita, and C. D. Lin, Phys. Rev. A **80**, 013401 (2009).

[32] A.-T. Le, R. R. Lucchese, and C. D. Lin, Phys. Rev. A **87**, 063406 (2013).

[33] A.-T. Le, R. D. Picca, P. D. Fainstein, D. A. Telnov, M. Lein, and C. D. Lin, J. Phys. B: At. Mol. Opt. Phys. **41**, 081002 (2008).

[34] A.-T. Le, H. Wei, C. Jin, and C. D. Lin, J. Phys. B: At. Mol. Opt. Phys. **49**, 053001 (2016).

[35] R. R. Lucchese, G. Raseev, and V. McKoy, Phys. Rev. A **25**, 2572 (1982).

[36] R. E. Stratmann and R. R. Lucchese, J. Chem. Phys. **102**, 8493 (1995).

[37] M. B. Gaarde, J. L. Tate, and K. J. Schafer, J. Phys. B: At. Mol. Opt. Phys. **41**, 132001 (2008).

[38] K. J. Schafer and K. C. Kulander, Phys. Rev. Lett. **78**, 638 (1997).

[39] M. B. Gaarde, F. Salin, E. Constant, P. Balcou, K. J. Schafer, K. C. Kulander, and A. L'Huillier, Phys. Rev. A **59**, 1367 (1999).

[40] P. Salières, A. L'Huillier, and M. Lewenstein, Phys. Rev. Lett. **74**, 3776 (1995).

[41] M. Bellini, C. Lyngå, A. Tozzi, M. B. Gaarde, T. W. Hänsch, A. L'Huillier, and C.-G. Wahlström, Phys. Rev. Lett. **81**, 297 (1998).

[42] D. Shafir, B. Fabre, J. Higuet, H. Soifer, M. Dagan, D. Descamps, E. Mével, S. Petit, H. J. Wörner, B. Pons, et al., Phys. Rev. Lett. **108**, 203001 (2012).

[43] E. W. Larsen, S. Carlström, E. Lorek, C. M. Heyl, D. Paleček, K. J. Schafer, A. L'Huillier, D. Zigmantas, and J. Mauritsson, Sci. Rep. **6** (2016).

[44] R. Abrines and I. C. Percival, Proc. Phys. Soc. **88**, 861 (1966).

[45] P. J. Ho, R. Panfili, S. L. Haan, and J. H. Eberly, Phys. Rev. Lett. **94**, 093002 (2005).

[46] S. L. Haan, L. Breen, A. Karim, and J. H. Eberly, Phys. Rev. Lett. **97**, 103008 (2006).

[47] C. Lemell, J. Burgdörfer, S. Gräfe, K. I. Dimitriou, D. G. Arbó, and X.-M. Tong, Phys. Rev. A **87**, 013421 (2013).

[48] C. A. Mancuso, D. D. Hickstein, K. M. Dorney, J. L. Ellis, E. Hasović, R. Knut, P. Grychtol, C. Gentry, M. Gopalakrishnan, D. Zusin, et al., Phys. Rev. A **93**, 053406 (2016).

[49] P. M. Abanador, F. Mauger, K. Lopata, M. B. Gaarde, and K. J. Schafer, J. Phys. B: At. Mol. Opt. Phys. **50**, 035601 (2017).

[50] D. J. W. Hardie and R. E. Olson, J. Phys. B: At. Mol. Opt. Phys. **16**, 1983 (1983).

[51] P. Botheron and B. Pons, Phys. Rev. A **80**, 023402 (2009).

[52] K. S. Budil, P. Salières, A. L'Huillier, T. Ditmire, and M. D. Perry, Phys. Rev. A **48**, R3437 (1993).

[53] P. Dietrich, N. H. Burnett, M. Ivanov, and P. B. Corkum, Phys. Rev. A **50**, R3585 (1994).

[54] M. Möller, Y. Cheng, S. D. Khan, B. Zhao, K. Zhao, M. Chini, G. G. Paulus, and Z. Chang, Phys. Rev. A **86**, 011401 (2012).

[55] S. D. Khan, Y. Cheng, M. Möller, K. Zhao, B. Zhao, M. Chini, G. G. Paulus, and Z. Chang, Appl. Phys. Lett. **99**, 161106 (2011).

[56] J.-W. Geng, L. Qin, M. Li, W.-H. Xiong, Y. Liu, Q. Gong, and L.-Y. Peng, J. Phys. B: At. Mol. Opt. Phys. **47**, 204027 (2014).

[57] J. A. Hostetter, J. L. Tate, K. J. Schafer, and M. B. Gaarde, Phys. Rev. A **82**, 023401 (2010).

[58] H. Soifer, P. Botheron, D. Shafir, A. Diner, O. Raz, B. D. Bruner, Y. Mairesse, B. Pons, and N. Dudovich, Phys. Rev. Lett. **105**, 143904 (2010).

[59] J. Higuet, H. Ruf, N. Thiré, R. Cireasa, E. Constant, E. Cormier, D. Descamps, E. Mével, S. Petit, B. Pons, et al., Phys. Rev. A **83**, 053401 (2011).

[60] F. Cloux, B. Fabre, and B. Pons, Phys. Rev. A **91**, 023415 (2015).

[61] M. J. Rakovic, D. R. Schultz, P. C. Stancil, and R. K. Janev, J. Phys. A: Math. Gen. **34**, 4753 (2001).

[62] R. H. Landau, M. J. Páez, and C. C. Bordeianu, *A Survey of Computational Physics* (Princeton University Press, Princeton, NJ, 2008).

[63] H. G. Muller, Phys. Rev. A **60**, 1341 (1999).

[64] C. Lyngå, M. B. Gaarde, C. Delfin, M. Bellini, T. W. Hänsch, A. L' Huillier, and C.-G. Wahlström, Phys. Rev. A **60**, 4823 (1999).

[65] P. Cvitanović, R. Artuso, R. Mainieri, G. Tanner, and G. Vattay, *Chaos: Classical and Quantum* (Niels Bohr Inst., Copenhagen, 2016).

[66] S. Huang, C. Chandre, and T. Uzer, J. Phys. B: At. Mol. Opt. Phys. **41**, 035604 (2008).

[67] A. Kamor, F. Mauger, C. Chandre, and T. Uzer, Phys. Rev. Lett. **110**, 253002 (2013).

[68] J. R. Cary and J. D. Hanson, Phys. Fluids **29**, 2464 (1986).

[69] A. Kamor, C. Chandre, T. Uzer, and F. Mauger, Phys. Rev. Lett. **112**, 133003 (2014).

[70] P. M. Abanador, F. Mauger, K. Lopata, M. B. Gaarde, and K. J. Schafer, Phys. Rev. A **97**, 043414 (2018).

[71] J. B. Watson, A. Sanpera, D. G. Lappas, P. L. Knight, and K. Burnett, Phys. Rev. Lett. **78**, 1884 (1997).

[72] S. Larochelle, A. Talebpour, and S. L. Chin, J. Phys. B: At. Mol. Opt. Phys. **31**, 1201 (1998).

[73] C. Ruiz, L. Plaja, L. Roso, and A. Becker, Phys. Rev. Lett. **96**, 053001 (2006).

[74] B. Bergues, M. Kübel, N. G. Johnson, B. Fischer, N. Camus, K. J. Betsch, O. Herrwerth, A. Senftleben, A. M. Sayler, T. Rathje, et al., Nature Commun. **3**, 813 (2012).

[75] P. Kruit, J. Kimman, H. G. Muller, and M. J. van der Wiel, Phys. Rev. A **28**, 248 (1983).

[76] G. G. Paulus, W. Nicklich, H. Xu, P. Lambropoulos, and H. Walther, Phys. Rev. Lett. **72**, 2851 (1994).

[77] J. S. Parker, L. R. Moore, K. J. Meharg, D. Dundas, and K. T. Taylor, J. Phys. B: At. Mol. Opt. Phys. **34**, L69 (2001).

[78] A. L'Huillier, L. A. Lompre, G. Mainfray, and C. Manus, Phys. Rev. A **27**, 2503 (1983).

[79] D. N. Fittinghoff, P. R. Bolton, B. Chang, and K. C. Kulander, Phys. Rev. Lett. **69**, 2642 (1992).

[80] B. Walker, B. Sheehy, L. F. DiMauro, P. Agostini, K. J. Schafer, and K. C. Kulander, Phys. Rev. Lett. **73**, 1227 (1994).

[81] U. Eichmann, M. Dörr, H. Maeda, W. Becker, and W. Sandner, Phys. Rev. Lett. **84**, 3550 (2000).

[82] J. Ullrich, R. Moshammer, A. Dorn, R. Dörner, L. P. H. Schmidt, and H. Schmidt-Böcking, Rep. Prog. Phys. **66**, 1463 (2003).

[83] T. Weber, M. Weckenbrock, A. Staudte, L. Spielberger, O. Jagutzki, V. Mergel, F. Afaneh, G. Urbasch, M. Vollmer, H. Giessen, et al., Phys. Rev. Lett. **84**, 443 (2000).

[84] R. Moshammer, B. Feuerstein, W. Schmitt, A. Dorn, C. D. Schröter, J. Ullrich, H. Rottke, C. Trump, M. Wittmann, G. Korn, et al., Phys. Rev. Lett. **84**, 447 (2000).

[85] C. F. de Morisson Faria and X. Liu, J. Mod. Opt. **58**, 1076 (2011).

[86] T. Weber, H. Giessen, M. Weckenbrock, G. Urbasch, A. Staudte, L. Spielberger, O. Jagutzki, V. Mergel, M. Vollmer, and R. Dörner, Nature **405**, 658 (2000).

[87] B. Feuerstein, R. Moshammer, D. Fischer, A. Dorn, C. D. Schröter, J. Deipenwisch, J. R. Crespo Lopez-Urrutia, C. Höhr, P. Neumayer, J. Ullrich, et al., Phys. Rev. Lett. **87**, 043003 (2001).

[88] V. B. de Jesus, B. Feuerstein, K. Zrost, D. Fischer, A. Rudenko, F. Afaneh, C. D. Schröter, R. Moshammer, and J. Ullrich, J. Phys. B: At. Mol. Opt. Phys. **37**, L161 (2004).

[89] Y. Liu, S. Tschuch, A. Rudenko, M. Dürr, M. Siegel, U. Morgner, R. Moshammer, and J. Ullrich, Phys. Rev. Lett. **101**, 053001 (2008).

[90] W. Becker, X. Liu, P. J. Ho, and J. H. Eberly, Rev. Mod. Phys. **84**, 1011 (2012).

[91] K. K. Hansen and L. B. Madsen, Phys. Rev. A **96**, 013401 (2017).

[92] M. Lein, E. K. U. Gross, and V. Engel, Phys. Rev. Lett. **85**, 4707 (2000).

[93] J. Javanainen, J. H. Eberly, and Q. Su, Phys. Rev. A **38**, 3430 (1988).

[94] X. Andrade, D. Strubbe, U. De Giovannini, A. H. Larsen, M. J. T. Oliveira, J. Alberdi-Rodriguez, A. Varas, I. Theophilou, N. Helbig, M. J. Verstraete, et al., Phys. Chem. Chem. Phys. **17**, 31371 (2015).

[95] U. De Giovannini, A. H. Larsen, and A. Rubio, Eur. Phys. J. B **88**, 56 (2015).

[96] K. Burnett, V. C. Reed, J. Cooper, and P. L. Knight, Phys. Rev. A **45**, 3347 (1992).

[97] R. B. Blackman and J. W. Tukey, *The Measurement of Power Spectra* (Dover Publications, New York, 1958).

[98] C. C. Chirilă, I. Dreissigacker, E. V. van der Zwan, and M. Lein, Phys. Rev. A **81**, 033412 (2010).

[99] D. Dundas, K. T. Taylor, J. S. Parker, and E. S. Smyth, J. Phys. B: At. Mol. Opt. Phys. **32**, L231 (1999).

[100] I. Tikhomirov, T. Sato, and K. L. Ishikawa, Phys. Rev. Lett. **118**, 203202 (2017).

[101] D. K. Efimov, A. Maksymov, J. S. Prauzner-Bechcicki, J. H. Thiede, B. Eckhardt, A. Chacón, M. Lewenstein, and J. Zakrzewski, Phys. Rev. A **98**, 013405 (2018).

[102] Y.-B. Li, X. Wang, B.-H. Yu, Q.-B. Tang, G.-H. Wang, and J.-G. Wan, Sci. Rep. **6**, 37413 (2016).

[103] S. L. Haan, J. S. Van Dyke, and Z. S. Smith, Phys. Rev. Lett. **101**, 113001 (2008).

[104] F. Mauger, C. Chandre, and T. Uzer, Phys. Rev. Lett. **102**, 173002 (2009).

[105] F. Mauger, A. Kamor, C. Chandre, and T. Uzer, Phys. Rev. E **85**, 066205 (2012).

[106] J. Tate, T. Auguste, H. G. Muller, P. Salières, P. Agostini, and L. F. DiMauro, Phys. Rev. Lett. **98**, 013901 (2007).

[107] K. Schiessl, K. L. Ishikawa, E. Persson, and J. Burgdörfer, Phys. Rev. Lett. **99**, 253903 (2007).

[108] M. V. Frolov, N. L. Manakov, and A. F. Starace, Phys. Rev. Lett. **100**, 173001 (2008).

[109] S. Micheau, Z. Chen, A.-T. Le, and C. D. Lin, Phys. Rev. A **79**, 013417 (2009).

[110] F. Mauger, C. Chandre, and T. Uzer, Phys. Rev. Lett. **104**, 043005 (2010).

[111] P. Hohenberg and W. Kohn, Phys. Rev. **136**, B864 (1964).

[112] W. Kohn and L. J. Sham, Phys. Rev. **140**, A1133 (1965).

[113] E. Runge and E. K. U. Gross, Phys. Rev. Lett. **52**, 997 (1984).

[114] F. Calegari, A. Trabattoni, A. Palacios, D. Ayuso, M. C. Castrovilli, J. B. Greenwood, P. Decleva, F. Martín, and M. Nisoli, J. Phys. B: At. Mol. Opt. Phys. **49**, 142001 (2016).

[115] N. T. Maitra, J. Chem. Phys. **144**, 220901 (2016).

[116] C. A. Ullrich, J. Chem. Phys. **125**, 234108 (2006).

[117] N. T. Maitra, K. Burke, and C. Woodward, Phys. Rev. Lett. **89**, 023002 (2002).

[118] S. Kümmel and L. Kronik, Rev. Mod. Phys. **80**, 3 (2008).

[119] A. Castro, M. A. L. Marques, and A. Rubio, J. Chem. Phys. **121**, 3425 (2004).

[120] T. L. Beck, Rev. Mod. Phys. **72**, 1041 (2000).

[121] X. Andrade, J. Alberdi-Rodriguez, D. A. Strubbe, M. J. Oliveira, F. Nogueira, A. Castro, J. Muguerza, A. Arruabarrena, S. G. Louie, A. Aspuru-Guzik, et al., Journal of Physics: Condensed Matter **24**, 233202 (2012).

[122] J. R. Chelikowsky, N. Troullier, and Y. Saad, Phys. Rev. Lett. **72**, 1240 (1994).

[123] F. Gygi and G. Galli, Phys. Rev. B **52**, R2229 (1995).

[124] A. Wardlow and D. Dundas, Phys. Rev. A **93**, 023428 (2016).

[125] X. Chu and S.-I. Chu, Phys. Rev. A **63**, 023411 (2001).

[126] E. P. Fowe and A. D. Bandrauk, Phys. Rev. A **81**, 023411 (2010).

[127] X. Chu and S.-I. Chu, Phys. Rev. A **64**, 063404 (2001).

[128] J. P. Perdew and K. Schmidt, AIP Conference Proceedings **577**, 1 (2001).

[129] J. P. Perdew and A. Zunger, Phys. Rev. B **23**, 5048 (1981).

[130] U. De Giovannini, D. Varsano, M. A. L. Marques, H. Appel, E. K. U. Gross, and A. Rubio, Phys. Rev. A **85**, 062515 (2012).

[131] A. Sissay, P. Abanador, F. Mauger, M. Gaarde, K. J. Schafer, and K. Lopata, J. Chem. Phys. **145**, 094105 (2016).

[132] C. Legrand, E. Suraud, and P.-G. Reinhard, J. Phys. B: At. Mol. Opt. Phys. **35**, 1115 (2002).

[133] P. Klüpfel, P. M. Dinh, P.-G. Reinhard, and E. Suraud, Phys. Rev. A **88**, 052501 (2013).

[134] R. van Leeuwen and E. J. Baerends, Phys. Rev. A **49**, 2421 (1994).

[135] M. E. Casida and D. R. Salahub, J. Chem. Phys. **113**, 8918 (2000).

[136] R. Baer, E. Livshits, and U. Salzner, Annu. Rev. Phys. Chem. **61**, 85 (2010).

[137] M. Lein, N. Hay, R. Velotta, J. P. Marangos, and P. L. Knight, Phys. Rev. Lett. **88**, 183903 (2002).

[138] M. Lein, N. Hay, R. Velotta, J. P. Marangos, and P. L. Knight, Phys. Rev. A **66**, 023805 (2002).

[139] T. Kanai, S. Minemoto, and H. Sakai, Nature **435**, 470 (2005).

[140] C. Vozzi, F. Calegari, E. Benedetti, J.-P. Caumes, G. Sansone, S. Stagira, M. Nisoli, R. Torres, E. Heesel, N. Kajumba, et al., Phys. Rev. Lett. **95**, 153902 (2005).

[141] W. Boutu, S. Haessler, H. Merdji, P. Breger, G. Waters, M. Stankiewicz, L. Frasinski, R. Taieb, J. Caillat, A. Maquet, et al., Nature Phys. **4**, 545 (2008).

[142] A. Rupenyan, P. M. Kraus, J. Schneider, and H. J. Wörner, Phys. Rev. A **87**, 033409 (2013).

[143] G. L. Kamta and A. D. Bandrauk, Phys. Rev. A **71**, 053407 (2005).

[144] M. F. Ciappina, C. C. Chirilă, and M. Lein, Phys. Rev. A **75**, 043405 (2007).

[145] S. Haessler, J. Caillat, and P. Salières, J. Phys. B: At. Mol. Opt. Phys. **44**, 203001 (2011).

[146] H. J. Wörner, J. B. Bertrand, P. Hockett, P. B. Corkum, and D. M. Villeneuve, Phys. Rev. Lett. **104**, 233904 (2010).

[147] R. Torres, T. Siegel, L. Brugnera, I. Procino, J. G. Underwood, C. Altucci, R. Velotta, E. Springate, C. Froud, I. C. E. Turcu, et al., Phys. Rev. A **81**, 051802 (2010).

[148] A. Etches, M. B. Gaarde, and L. B. Madsen, Phys. Rev. A **84**, 023418 (2011).

[149] F. Rosca-Pruna and M. J. J. Vrakking, J. Chem. Phys. **116**, 6567 (2002).

[150] R. Torres, R. de Nalda, and J. P. Marangos, Phys. Rev. A **72**, 023420 (2005).

[151] L. Kleinman and D. M. Bylander, Phys. Rev. Lett. **48**, 1425 (1982).

[152] N. Troullier and J. L. Martins, Phys. Rev. B **43**, 1993 (1991).

[153] D. W. Turner et al., *Molecular Photoelectron Spectroscopy* (Wiley, London, 1970).

[154] K. J. Schafer, M. B. Gaarde, A. Heinrich, J. Biegert, and U. Keller, Phys. Rev. Lett. **92**, 023003 (2004).

[155] G. Gademann, F. Kelkensberg, W. K. Siu, P. Johnsson, M. B. Gaarde, K. J. Schafer, and M. J. J. Vrakking, New J. Phys. **13**, 033002 (2011).

[156] D. Azoury, M. Krüger, G. Orenstein, H. R. Larsson, S. Bauch, B. D. Bruner, and N. Dudovich, Nature Commun. **8**, 1453 (2017).

[157] M. Lein, P. P. Corso, J. P. Marangos, and P. L. Knight, Phys. Rev. A **67**, 023819 (2003).

[158] G. Doumy, J. Wheeler, C. Roedig, R. Chirla, P. Agostini, and L. F. DiMauro, Phys. Rev. Lett. **102**, 093002 (2009).

[159] J.-A. You, J. M. Dahlström, and N. Rohringer, Phys. Rev. A **95**, 023409 (2017).

[160] P. Mulholland and D. Dundas, Phys. Rev. A **97**, 043428 (2018).

Vita

Paul Abanador was born in Batangas City of the Batangas province, Philippines. He attended De La Salle University in Manila, Philippines and received a Bachelor of Science degree in Physics in May 2012. He began his doctoral study at Louisiana State University in 2013 under the supervision of Kenneth Schafer and Mette Gaarde. He is scheduled to receive the Doctor of Philosophy degree in Physics at the December 2018 commencement.